

PHOTOLUMINESCENCE FROM MEH-PPV AND DP-PPV IN BULK
AND ENCAPSULATED IN POROUS ALUMINA

by

Dong Feng Qi

B.Sc. Zhongshan University, Guangzhou, China, 1990

M.Sc. Jinan University, Guangzhou, China, 1993

A THESIS SUBMITTED IN PARTIAL FULFILLMENT OF

THE REQUIREMENTS FOR THE DEGREE OF

MASTER OF APPLIED SCIENCE

in

THE FACULTY OF GRADUATE STUDIES

DEPARTMENT OF PHYSICS AND ASTRONOMY

We accept this thesis as conforming

to the required standard

THE UNIVERSITY OF BRITISH COLUMBIA

September, 2001

© Dong Feng Qi, 2001

In presenting this thesis in partial fulfilment of the requirements for an advanced degree at the University of British Columbia, I agree that the Library shall make it freely available for reference and study. I further agree that permission for extensive copying of this thesis for scholarly purposes may be granted by the head of my department or by his or her representatives. It is understood that copying or publication of this thesis for financial gain shall not be allowed without my written permission.

Department of Physics & Astronomy
The University of British Columbia
Vancouver, Canada
Date August 31st, 2001

Abstract

Two PPV derivatives, MEH-PPV and DP-PPV, are encapsulated in the nanopores of anodized alumina with different pore sizes (50/200 nm) and depth (10/60 μm). Time-integrated and time resolved optical emission properties of these structures have been studied and compared with those of thin films of the polymers. Significant blue shifts of the PL spectra (0.034 eV-0.183 eV) are found in the porous materials as compared to the bulk. The relative intensity of the one-phonon assisted transition increases in comparison with the intensity of the no-phonon transition in the nanostructured samples.

The time constants of the optical emission from the bulk MEH-PPV film are very similar in their energy dependence to results obtained previously on bulk PPV films when considered with respect to the excess energy above the peak of the emission spectrum. The decay times are, however, two to three times shorter in the parent. The energy dependence of the time constants measured in DP-PPV films and DP-PPV encapsulated in nanopores (pore diameter 200 nm, pore depth 60 μm) are also very similar to each other, and to the results obtained on the MEH-PPV. These results suggest that the intrachain diffusion of electron-hole excitations in all of these polymers, either in bulk or encapsulated form, is very similar.

Table of Contents

ABSTRACT	ii
TABLE OF CONTENTS	iii
LIST OF FIGURES	v
LIST OF TABLES	viii
ACKNOWLEDGEMENTS	ix
CHAPTER 1 INTRODUCTION	1
CHAPTER 2 THEORY	5
2.1 SUM FREQUENCY GENERATION AND UPCONVERSION	5
2.2 OPTICAL PROPERTIES OF CONJUGATED POLYMERS	11
CHAPTER 3 EXPERIMENT AND SAMPLE PREPARATION	14
3.1 OPTICAL SYSTEM OVERVIEW	14
3.2 MAJOR CHALLENGES AND SOLUTIONS	19
3.2.1 GENERAL ALIGNMENT	19
3.2.2 GATE AND PL SPOT WALK-OFF ON UPCONVERSION CRYSTAL	19
3.2.3 SHAPE OF EXCITATION SPOT	20
3.2.4 NONLINEAR CRYSTAL FOR UPCONVERSION	20
3.2.5 GATE AND PL BEAM GEOMETRY	21
3.2.6 PMT DARK CURRENT	23
3.2.7 LN/CCD AS A DETECTOR FOR EXTREMELY WEAK SIGNALS	23
3.3 UPCONVERSION DATA ACQUISITION	25
3.3.1 THE ZERO DELAY POINT: LASER UPCONVERSION	25
3.3.2 ALIGNMENT OF COLLECTION OPTICS	27
3.3.3 MAXIMIZING THE INTENSITY OF PL	28
3.3.4 THE SUM FREQUENCY SIGNAL	28
3.3.5 DATA COLLECTION	29
3.3.6 WHITE LIGHT UPCONVERSION	30
3.4 SAMPLE PREPARATION	32
3.4.1 BULK SAMPLES: FILM ON MICROSCOPE-SLIDES	32
3.4.2 HOST MATERIAL PREPARATION	34
3.4.3 ENCAPSULATING MEH-PPV INTO ANODIZED ALUMINA OR ANODISC	39
3.4.4 ENCAPSULATING DP-PPV INTO ANODIZED ALUMINA OR ANODISC	39

CHAPTER 4 EXPERIMENTAL RESULTS	40
4.1 TIME-INTEGRATED SPECTRA	41
4.1.1 EFFECTS OF NANOPOROUS HOSTS	41
4.1.2 TEMPERATURE DEPENDENCE	47
4.1.3 EXCITATION INTENSITY DEPENDENCE	48
4.1.4 COMPARISON OF PL INTENSITY FROM DIFFERENT SAMPLES	49
4.1.5 PHOTODEGRADATION.....	50
4.2 TIME-RESOLVED SPECTRA	54
4.2.1 PHASE-MATCHING CALIBRATION	54
4.2.2 BULK MEH-PPV	57
4.2.3 BULK DP-PPV	64
4.2.4 ANODISC DP-PPV	68
4.2.5 BULK VS. ANODISC DP-PPV: LIFETIME DEPENDENCE ON ENERGY	72
4.2.6 BULK MEH-PPV VS. BULK PPV: LIFETIME DEPENDENCE ON ENERGY	73
4.2.7 LIFETIME DEPENDENCE ON ENERGY FOR PPV AND DERIVATIVES.....	74
CHAPTER 5 SUMMARY AND CONCLUSIONS	75
5.1 SUMMARY	75
5.1.1 EXPERIMENTAL APPARATUS	75
5.1.2 EFFECTS OF ENCAPSULATION ON THE TIME-INTEGRATED LUMINESCENCE SPECTRUM OF MEH-PPV AND DP-PPV AT 77 K.....	76
5.1.3 EFFECTS OF ENCAPSULATION ON THE TIME-RESOLVED LUMINESCENCE SPECTRUM OF MEH-PPV AND DP-PPV AT 77 K.....	77
5.2 CONCLUSIONS.....	78
REFERENCE	80
APPENDIX A	82
APPENDIX B.....	84
APPENDIX C.....	86

List of Figures

1.1: Chemical structure of PPV, MEH-PPV and DP-PPV.....	2
2.1: Schematic optical setup of sum frequency experiment using a nonlinear crystal.....	5
2.2: Optics of an uniaxial crystal.....	7
2.3: Negative uniaxial crystal.....	8
2.4: Geometry of the gate and PL beams for determination of phase matching.....	10
2.5: Photoluminescence processes of organic molecules.....	11
2.6: Schematic diagram showing the segments of polymer chain.....	13
3.1: Schematic set-up for femto-second time-resolved photoluminescence spectroscopy.....	18
3.2: Polar plot of the phase matching angle as a function of the PL wavelength.....	21
3.3: The angular difference between the sum frequency propagation and the gate propagation as a function of PL wavelength under phase matched conditions.....	22
3.4: Schematic Setup for White Light Upconversion.....	31
3.5: Synthesis of MEH-PPV.....	33
3.6: Synthesis of DP-PPV.....	33
3.7: Set-up for Anodization of Aluminum.....	34
3.8: Schematic graph of sample before and after anodizing.....	35
3.9: SEM pictures of anodized alumina on aluminum foil.....	36
3.10: Pores of Anodisc.....	37
3.11: Chemical reaction route of silanization of Anodisc.....	38

4.1: Photoluminescence Spectra of bulk MEH-PPV and bulk DP-PPV at 77 K	41
4.2: Photoluminescence Spectra of Anodisc MEH-PPV and Anodisc DP-PPV at 77 K	42
4.3: Two-Gaussian fits for bulk MEH-PPV and bulk DP-PPV PL at 77 K and three-Gaussian fits for bulk MEH-PPV and bulk DP-PPV PL at 77 K.....	44
4.4: Two-Gaussian fits for Anodisc MEH-PPV and Anodisc DP-PPV PL at 77 K and three-Gaussian fits for Anodisc MEH-PPV and Anodisc DP-PPV PL at 77 K	45
4.5: Normalized 77 K PL spectra of MEH-PPV and DP-PPV.....	46
4.6: Effects of Temperature on the time-integrated photoluminescence of bulk DP-PPV, Anodized DP-PPV and bulk MEH-PPV	47
4.7: Intensity of bulk DP-PPV PL at 77 K versus excitation intensity	48
4.8: 77 K Photoluminescence spectra of MEH-PPV and DP-PPV in bulk and nanostructured forms	49
4.9: Evolution of Spectra of Anodisc MEH-PPV and Anodisc DP-PPV with excitation time.....	52
4.10: Photo-Degradation of Anodisc MEH-PPV and Anodisc DP-PPV	53
4.11: White Light Upconversion spectra at different crystal orientation angles	55
4.12: Wavelength at which the mixing efficiency is maximum for a given angular position of the nonlinear crystal	56
4.13: Short time regime of time-resolved bulk MEH-PPV photoluminescence at 77 K.....	58
4.14: Bi-exponential fits of time-resolved bulk MEH-PPV photoluminescence at 77 K.....	59
4.15: Time constants extracted from the time-resolved decay profiles using the Bi-exponential fits.	60
4.16: Population lifetime versus estimated electronic energy	61
4.17: Population lifetime versus ECL energy for bulk PPV	63
4.19: Extracted time constants versus probe energy for bulk DP-PPV PL at 77 K.....	65
4.18: Time-resolved profiles for bulk DP-PPV photoluminescence at 77 K.....	66
4.20: Population Lifetime versus estimated ECL energy	67
4.22: Extracted time constants versus probe energy for Anodisc DP-PPV PL at 77 K.....	69

4.21: Decay profiles for Anodisc DP-PPV photoluminescence at 77 K.....	70
4.23: Population Lifetime versus estimated ECL energy for Anodisc DP-PPV.....	71
4.24: Comparison of population lifetimes of bulk and Anodisc DP-PPV.....	72
4.25: Comparison of population lifetimes of bulk PPV and bulk MEH-PPV.....	73
4.26: Comparison of population lifetimes of PPV and its derivatives	74

List of Tables

Table 1.1 Full names of the polymers studied.....	2
Table 3.1 Specifications of optical components in Figure 3.1	17
Table 4.1 Sample Properties and Sample Labels	40
Table 4.2 Comparison of Spectra of Bulk and Nanostructured MEH-PPV and DP-PPV	43

Acknowledgements

I would like to thank my supervisor Dr. Jeff F. Young for his continuous guidance and encouragement in the past two years. I am so fortunate to have worked with him, through whom I could expose myself to the academic and industrial atmosphere of Canada and North America. I am also in debt to Dr. Katja Rademacher, Mr. Andras Pattantyus and Ms. Keri Kwong in Dr. Michael O. Wolf's group in Chemistry Department of UBC for preparing various conjugated polymer samples used in this thesis. I would also like to thank all my colleagues in Photonics Nanostructures Lab, especially Mr. Alex Busch, Dr. Xiaonong Shen and Ms. Lilian Fan, for their constructive discussion and resourceful help.

In addition, I would like to sincerely thank my dear wife Qiaomin, for her full support through out my graduate study in UBC, my mother Shaowen, who flow from China to Vancouver, helping me take care of my new born son, so that I could concentrate on the research work.

dedicated to Qiaomin, Hao, Ming-Hau and Wing-Hau

Chapter 1

Introduction

Conjugated polymers have been the subject of intensive research in the last twenty years, mainly due to their semiconductor-like optical and electronic properties. These organic materials offer promise for use in opto-electronic devices such as organic light emitting diodes (OLEDs) [1], light emitting electrochemical cells [2], photodiodes [3], sensors [18], waveguides [5] and lasers [6], etc. As compared to the traditional inorganic semiconductors, such as GaAs, conjugated polymer based devices are easier to fabricate. Currently, full color OLED based products are commercially available, such as cell phone displays [7].

However, the lifetime of such conjugated-polymer-based products, e.g. the OLED display, is much shorter as compared to the LCD/CRT based display and yields for manufacturing are inconsistent. For example, LCDs tend to operate for 10,000 to 15,000 hours, but OLEDs last only 5,000 hours [8]. Research is needed to find new materials and structures to improve the device performance, to increase the device lifetime and make the device more robust. To do that, conjugated polymers have been mixed with nanoparticles such as C_{60} [9,32], carbon nanotubes [10], CdS [11] and TiO_2 [12], etc. to form polymer-nanoparticle-composites. Conjugated polymers are also encapsulated in nanoporous materials, such as porous silica [13,14,23,31] or porous GaP [21], to modify their optical properties

In this thesis, the optical properties of PPV derivatives, MEH-PPV and DP-PPV are compared in bulk form and when encapsulated in the nanopores of anodized alumina. The samples were synthesized by members of Dr. M.O. Wolf's research group in the Chemistry

Department of UBC. Figure 1.1 shows the chemical structures of PPV, MEH-PPV and DP-PPV. The full names for them are given in Table 1.1. The polymers are prepared in two forms, bulk form, by spin-coating from the polymer solutions onto microscopic glass and nanostructured form, by encapsulating the polymer into porous alumina.

Table 1.1 Full names of the polymers studied

Abbreviation	Full Name
PPV	<i>poly(p-phenylenevinylence)</i>
MEH-PPV	<i>poly(1-methoxy-4-(2-ethylhexyloxy-2, 5-phenylenevinylene)</i>
DP-PPV	<i>poly(2,3-diphenyl-p-phenylenyvinylene)</i>

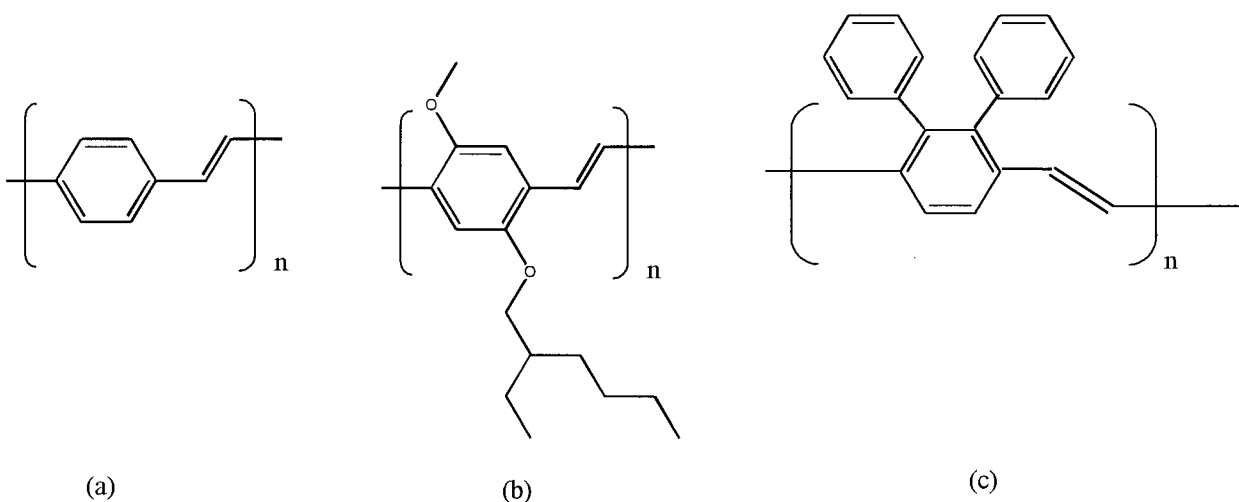


Figure 1.1: Chemical structures of (a) PPV, (b) MEH-PPV, and (c) DP-PPV.

This thesis reports a study of the time-integrated and time-resolved optical emission properties of these samples, predominantly obtained at 77 K. Owing to the relatively weak emission from these, as compared to bulk PPV samples, modifications had to be made to the time-resolved optical detection system originally developed by McCutcheon [18] for studying bulk PPV. Chapter 2 describes some of the basic optical properties of the materials used in the nonlinear optical sum-frequency system and the polymers themselves. Chapter 3 describes how the time-resolved photoluminescence system was modified in order to increase its sensitivity by more than a factor of three times.

Chapter 4 presents the time-integrated and time-resolved results obtained in bulk and nanostructured MEH-PPV and DP-PPV, and compares them with those previously obtained from bulk PPV. The bulk spectra of the three types of polymer are all similarly shaped, but are centered at different wavelengths in the visible part of the spectrum. The energy dependence of the decay time constants obtained from the time-resolved experiments are remarkably similar for all samples when the energy scales are shifted so the peaks of the emission spectra overlap. These time constants decrease almost exponentially with excess energy above the peak in the density of states associated with the inhomogeneously broadened distribution of coherent segment lengths in the polymer chains. While these dynamics are similar in bulk and nanostructured forms of the polymers, the time-integrated spectra are changed significantly when the polymers are encapsulated in the nanoporous material. Chapter 4 summarizes the blue shifts, broadening, and shape changes that occur in these time-integrated spectra from the nanostructured samples.

In Chapter 5, the conclusions drawn from the experimental results are summarized and some future work is suggested. Together with the previous work on bulk PPV, the present results motivate further, more detailed studies of PPV-based polymers encapsulated in nanoporous alumina. The aim of these studies should be to understand better the interaction of the polymers with the pore walls, and how they influence their optical properties. Appendix A and B present the Maple code to numerically calculate the phase matching conditions for the sum frequency generation. Appendix C presents the chemical process to silanizing the anodized alumina.

Chapter 2

Theory

2.1 Sum Frequency Generation and Upconversion

The sum frequency generation technique based on non-linear optical crystals was first used by Mahr and Hirsch [16] in 1975. J. Shah has given a detailed review in 1988 on this

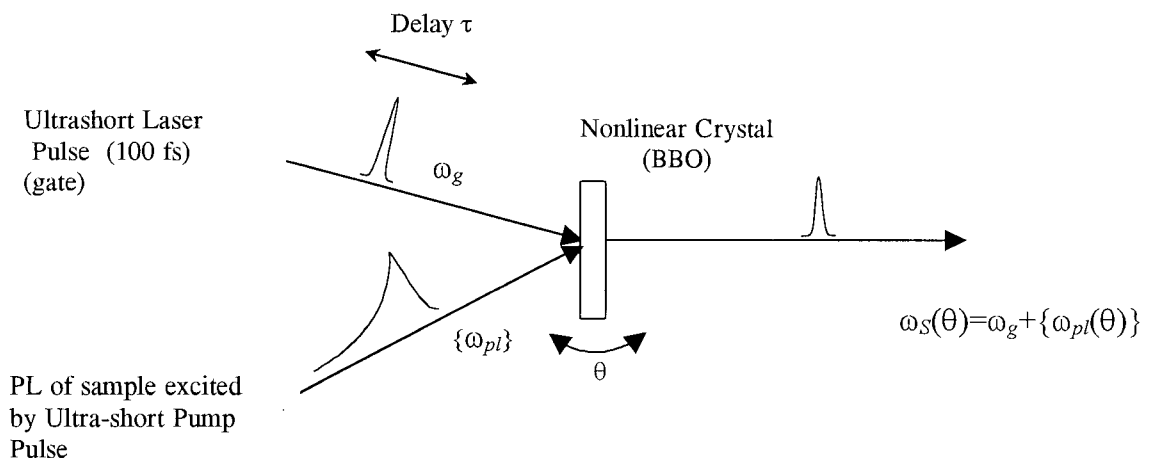


Figure 2.1: Schematic optical setup of sum frequency experiment using a nonlinear crystal.

technique [17], which is shown schematically in Figure 2.1. The photoluminescence (PL) excited by an ultra-short pump pulse* is mixed with an ultra-short gate pulse in a properly oriented non-linear crystal, such as beta-barium borate, β -BaB₂O₄ (BBO), to generate sum frequency radiation. There are two conditions to be satisfied for efficient sum frequency generation.

* The ultra-short pump pulse originates from the ultra-short laser pulse by frequency doubling.

The mixing process only takes place when both the PL and gate pulses are present and interact in the crystal at exactly the same time. This can be achieved by varying and monitoring the light-path lengths of the ultra-short laser pulse (gate) and the ultra-short pump pulse (excitation/PL) beams, as described in Chapter 3. This is the condition that allows the technique to be used to achieve ultrafast time resolution. However, even if the PL and gate beams temporally and spatially overlap in the crystal, a sum frequency signal will only be generated if the two are “phase matched”. The phase matching condition is given by equations (2.1) and (2.2).

$$\omega_g + \omega_{pl} = \omega_s \quad (2.1)$$

$$\vec{k}_g + \vec{k}_{pl} = \vec{k}_s \quad (2.2)$$

where ω_g , ω_{pl} and ω_s are the frequencies of the gate, PL and sum frequency beams respectively, and \vec{k}_g , \vec{k}_{pl} and \vec{k}_s are the corresponding wave vectors of the gate, PL and sum frequency beams in the nonlinear crystal.

To simplify the analysis, we consider a collinear phase matching, which requires,

$$k_g + k_{pl} = k_s \quad (2.3)$$

In terms of the refractive indices $n(\omega)$, (2.3) can be written as [15]

$$\omega_g [n(\omega_s) - n(\omega_g)] + \omega_{pl} [n(\omega_s) - n(\omega_{pl})] = 0 \quad (2.4)$$

In transparent isotropic materials with normal dispersion, the index of refraction $n(\omega)$ increases with ω , so the above relation can never be satisfied. By using a negative uniaxial crystal, such as BBO, and choosing the ω_s beam to be polarized in the extraordinary direction, it is possible to arrange for $n(\omega_s) - n(\omega_g)$ and $n(\omega_s) - n(\omega_{pl})$ to have opposite signs. Two types

of phase matching are commonly used. In type I, both $n(\omega_g)$ and $n(\omega_{pl})$ are ordinary. In type II, either $n(\omega_g)$ or $n(\omega_{pl})$ is ordinary [15].

To further understand the mechanism of sum frequency generation using negative uniaxial crystals, such as BBO, one should know the optics of the uniaxial crystals, which was

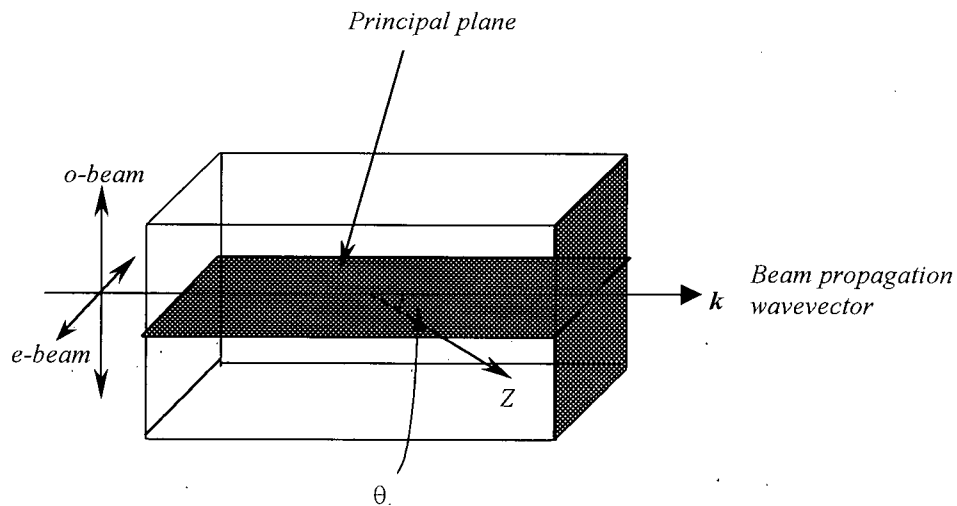


Figure 2.2: Optics of uniaxial crystals.

described in Reference [33]. As shown in Figure 2.2, in *uniaxial crystals*, there exists a specific direction called the *optic axis* (the Z axis). The plane containing the Z axis and the wave vector of the light wave is termed the *principal plane*. The light beam whose polarization is normal to the principal plane is called an *ordinary beam* or an *o-beam*. The beam polarized in the principal plane is called an *extraordinary beam* or *e-beam*. The refractive index of the *o-beam*, which is denoted by n_o , does not depend on the propagation direction, while the refractive index of the *e-beam* depends on the propagation direction. The difference between the refractive indices of the ordinary and extraordinary beams is known as the *birefringence* Δn . The value of Δn is zero along the optic axis Z and reaches a maximum, $\Delta n = n_o - n_e$ in the direction normal to the Z axis.

In an uniaxial crystal, the index of refraction of the *e-beam*, $n_{e\text{-beam}}(\theta)$ depends on the angle between the propagation beam and the *Z* axis, denoted as θ , as shown in Figure 2.2-2.3, and is determined by the ellipse defined by n_o and n_e , the *principal values* of the refractive indices [33].

In this work, non-collinear type I phase matching was used, with both the gate and PL beams polarized as *o-beams*. Upconversion was accomplished in a negative ($n_o > n_e$) uniaxial BBO crystal cut at an angle $\theta_{\text{cut}} = 38^\circ$ with respect to the optic axis (the *Z* axis) as shown in Figure 2.3.

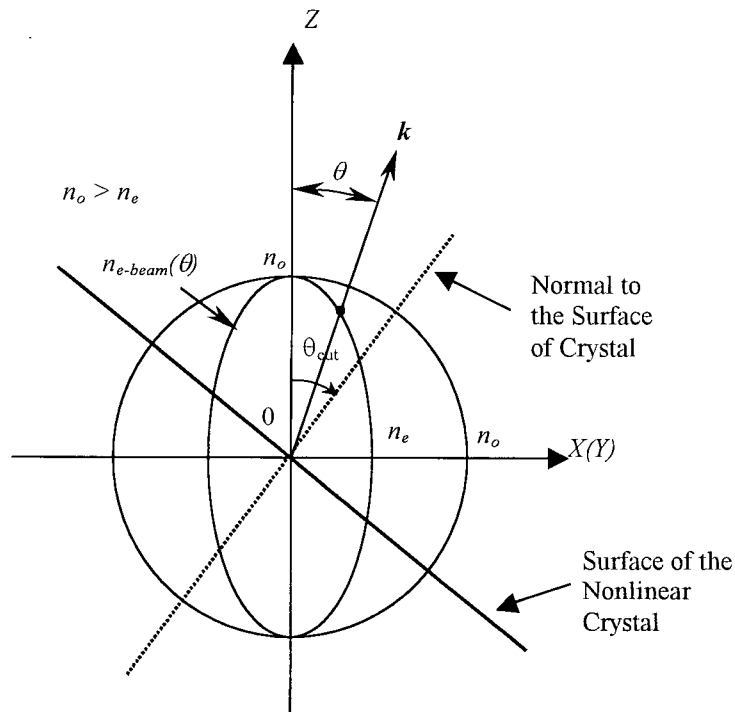


Figure 2.3: Negative uniaxial crystal: Principal values of refractive indices. Index ellipse. Cut angle with respect to the optic axis.

As shown in Figure 2.4, the gate and PL beams are not collinear. To achieve phase matching for such a geometry, the nonlinear crystal must be oriented to the right phase matching angle, which is given by [17] [18]

$$\sin^2(\theta_m) = \frac{(n_s(\theta_m))^{-2} - (n_o^s)^{-2}}{(n_e^s)^{-2} - (n_o^s)^{-2}} \quad (2.5)$$

where θ_m is the phase matching angle (the internal angle between sum frequency wave vector and the optical Z axis of the nonlinear crystal), n_e^s and n_o^s refer to the principal values of refractive index at the sum frequency ω_s , respectively, and $n_s(\theta_m)$ is determined by

$$n_s = k_s c / \omega_s \quad (2.6)$$

where ω_s is determined by (2.1), k_s is given by equation (2.2), and k_g and k_{pl} are magnitudes of the gate and the PL wave vectors inside the nonlinear crystal, determined by (for Type I phase matching)

$$k_g = n_g^o \omega_g / c \quad (2.7)$$

$$k_{pl} = n_{pl}^o \omega_{pl} / c \quad (2.8)$$

where n_g^o and n_{pl}^o are the ordinary indices of the gate and PL inside the nonlinear crystal. The indices of refraction, n_g^o and n_{pl}^o , are wavelength dependent but are simply determined by using the empirical dispersion relations given in Reference [33] for BBO. Referring to Figure 2.4, the external angle between the gate and PL beams ($\theta_{1i} + \theta_{2i}$) can be easily obtained by using the method described in Chapter 3. The internal angle between the gate and PL beams ($\theta_{1t} + \theta_{2t}$) is determined by refraction at the interface according to Snell's law. Based on the equations (2.1), (2.2) and (2.5)-(2.8), McCutcheon [18] developed a useful Maple code to find

numerically the incident angle of the PL beam, θ_{1i} , required to phase match a specific frequency component of the PL. This code was used throughout this thesis work and it was modified to extract the angular difference between the sum frequency propagation and the gate propagation under phase matching conditions. The Maple codes are attached in Appendix A and B. A more detailed description of the code can be found in the Appendix of Reference [18].

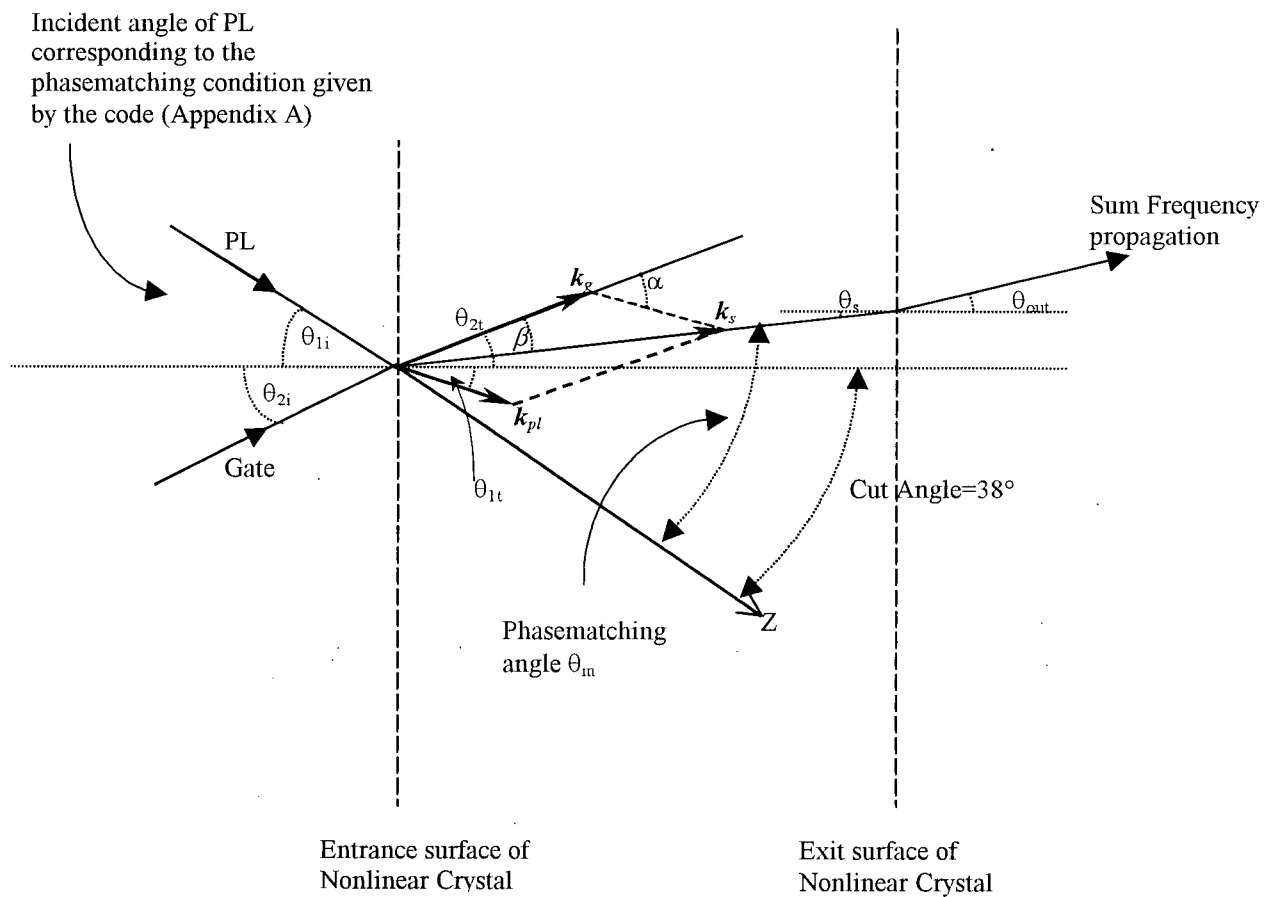


Figure 2.4: Geometry of the gate and PL beams for determination of phase matching.

2.2 Optical Properties of Conjugated Polymers

Conjugated polymers exhibit many semiconductor-like properties. However, the optical

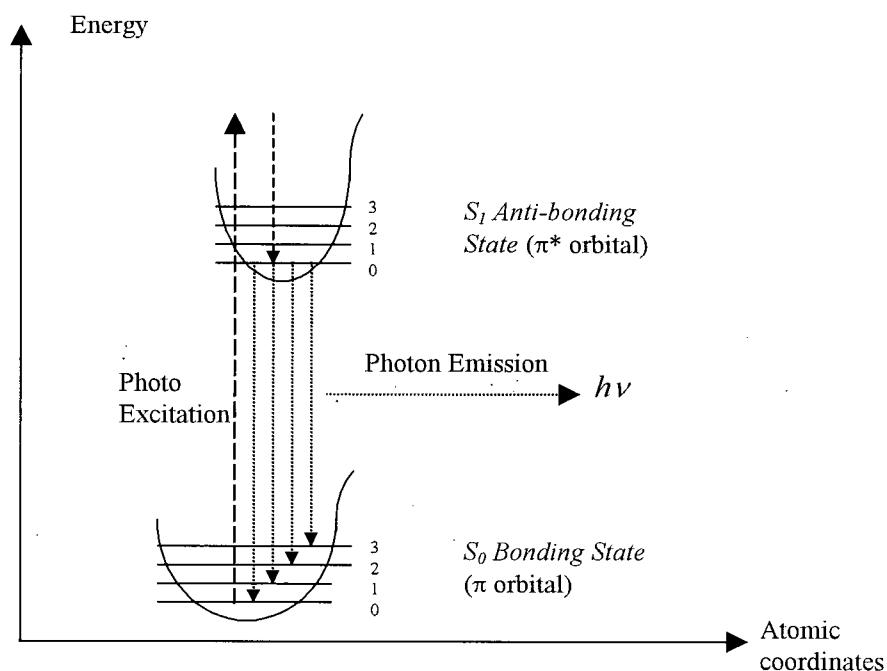


Figure 2.5: Photoluminescence processes between the S_0 and S_1 electronic states of organic molecule.

properties are more conveniently described by a molecular picture, which was outlined in Reference [26] by Greenham and Friend.

First consider a single isolated benzene ring (C_6H_6), which ultimately forms part of the backbone of the polymer chain. The electronic structure can be conveniently described in terms of σ bonds formed by overlap of sp^2 hybrid orbitals and π bonding formed by overlap of p_z orbitals on adjacent carbon atoms. The σ orbitals are relatively deep bonding orbitals. The semiconductor-like properties of conjugated polymer arise from the delocalization of the relatively shallow π orbital electrons. The π states in the benzene molecule act very much like

the valence (bonding π orbital) and conduction (anti-bonding π^* orbital) states in inorganic semiconductors, such as GaAs. The promotion of electrons from occupied π to unoccupied π^* states typically results in a change in the quasi equilibrium geometry of the molecule. The transitions associated with photoluminescence from an organic molecule can be represented as in Figure 2.5. The energies of the ground (π state) and excited (π^* state) states are shown as a function of the configuration coordinates of the molecule system, which represents the positions of the atomic nuclei. The parabolic shape of the energy bands indicates an energy increase due to displacements from the equilibrium configuration for a specific electronic state. Each electronic state is associated with a set of vibrational sublevels that are spaced much closer than the electronic energy levels. When the molecule is excited (absorption of high energy photons), electrons are promoted from the bottom of the S_0 state to high lying S_1 sublevels, from which they non-radiatively decay very quickly ($< 10^{-13}$ s) down to the bottom of S_1 . Radiative emission from S_1^0 can result from a transition to any one of the vibrational sublevels in S_0 . The transition from the bottom of S_1 to the bottom of S_0 is a purely electronic transition, and is denoted as $S_1 \rightarrow S_0 / 0 \rightarrow 0$ or $S_{0,0}$. The transition from the bottom of S_1 to the other vibrational sublevels in S_0 are denoted as $S_1 \rightarrow S_0 / 0 \rightarrow 1$, $S_1 \rightarrow S_0 / 0 \rightarrow 2, \dots$ etc.

Polymer chains are formed by bonding identical monomer molecules in a linear chain. When defect free, the π electrons can be delocalized over several monomers. The number of monomer units over which the orbitals are delocalized is determined by defects on the polymer chain, such as twists, bends or impurities, as shown schematically in Figure 2.6. The effective conjugation length (ECL) will determine the energy spacing of the S_0 and S_1 levels, and thus the emission energies from the segments [30]. The transition energy is smaller for longer

effective conjugation lengths and is larger for short effective conjugation lengths. The distribution of conjugation lengths, typically between 10 and 30 monomers [30], produces an inhomogeneously broadened density of states (DOS) distribution.

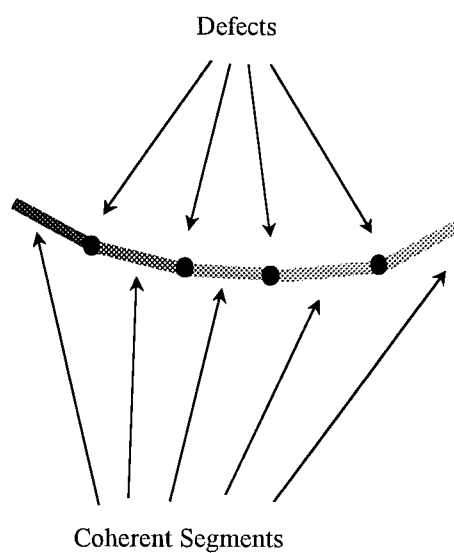


Figure 2.6: Schematic diagram showing the segments of a polymer chain jointed by defects such as twists, bends or impurities.

Chapter 3

Experiment and Sample Preparation

Reference [18] gives a detailed description of the basic upconversion system used in this work. This chapter will give a brief review and discuss the improvements made to optimize the pre-existing system to achieve a better sensitivity and to reduce the noise floor.

3.1 Optical System Overview

Figure 3.1 shows a schematic representation of the setup for the time-resolving experiment. A Spectra-Physics Mode-locked Titanium Sapphire (Ti:Sapph) laser is pumped by an Ar⁺ laser with a constant pumping power of 7 W. The Titanium Sapphire laser is tunable over a range of 735-820 nm with a maximum output power of 800 mW at 800 nm. When the laser system is well mode-locked, it emits ~ 100 femtosecond (full width at half maximum intensity, $\text{sech}^2(t)$ shaped) ultra-short laser pulses with a repetition rate of 82 MHz.

The Ti:Sapph laser beam is split by BS1 into an excitation beam and a gate beam. The gate beam first hits a retro-reflector mounted on a translation stage, then is directed by mirrors M3, M4, M5 and M8, and finally focused by L3 onto the surface of the non-linear crystal, C2, for upconversion. The excitation beam first hits M6 and another retro-reflector mounted on a mini-shaker whose frequency can be adjusted from 5 Hz to 30 Hz. This mini-shaker is useful in finding the zero delay point described later in section 3.3. Directed by M7, the excitation beam is focused by L1 onto a non-linear crystal C1 where it is frequency doubled to generate

UV pulses with the same repetition rate as the gate beam. The UV beam is directed by M9 and M10, and focused by L2 onto the sample in the cryostat. The photoluminescence excited by the UV pulse is collimated by a 90° parabolic mirror (PM), directed by M11/M12 and focused by L4 onto the same spot as the gate beam on crystal C2.

The sum frequency signal generated in C2 is collimated by L5, directed by M13/M14 and focused by L6 onto the entrance slit of the monochromator. Filter F1 is used to filter out the second harmonic background from the strong gate pulses (even though the crystal C1 is oriented to phase match ω_g and ω_{pl} , there is significant non-phase-matched second harmonic generation at $2\omega_g$ due to the strength of the gate beam). Photon counting is done by either a photo-multiplier tube (PMT) connected to a computer-monitored discriminator or a liquid nitrogen cooled CCD detector. Table 3.1 gives the major specifications of all the optical components used in the time-resolved photoluminescence experiments illustrated in Figure 3.1.

The whole experimental system is controlled by Labview programs via computer interfaces, including rotation of the non-linear crystal C2, pulse counting from the PMT discriminators and positioning the monochromator for a given detection wavelength. A CCD detector cooled by liquid nitrogen is also used for detecting very weak sum frequency signals. The CCD offers lower noise, but it is not as convenient as the PMT for measuring full spectra at a fixed delay. The PMT is made by Thorn EMI Electron Tubes Ltd. (Type: 9784A). The CCD is from Princeton Instruments Inc. (Model: Spec10:100BR).

The upconversion crystal C2 is mounted on a three-dimensional translation stage on top of a motor-driven rotation stage. The surface of the crystal is parallel to the x direction of the translation stage. Z and y directions are used to align the crystal so that the focused spots of the

gate and PL do not walk off when the crystal is rotated. A small piece of Teflon tape ($\sim 2 \times 4$ mm) is placed on the surface of the crystal to image PL and gate pulse spots. A Panasonic® CCD camera is used to view the surface of the crystal on a monitor.

The sample is mounted using Teflon tape at the end of a one-meter-long probe inserted down the center of the cryostat. The cryostat was designed to cool the samples to 77 K with liquid nitrogen or to 4 K with liquid Helium. Polymer samples studied in this thesis were cooled to 77 K to avoid photo-degradation.

Table 3.1 Specifications of optical components in Figure 3.1

Symbols in Figure 3.1	Specifications
M1-M8 M12	Newport Round Pyrex Mirror 25.4 mm Diameter, 1/5 wave, 0.5-18 μm
M11	50 \times 50 mm Square Flat Mirror, 1/5 wave, 0.5-18 μm
M9-M10	Newport Round Pyrex Mirror 25.4 mm Diameter, 1/5 wave, 250-600 nm
M13-M14	Newport Round Pyrex Mirror 50.8 mm Diameter, 1/5 wave, 250-600 nm
C1	5 \times 5 \times 0.5 mm Beta-Barium Borate (BBO) Crystal, cut [†] at $\theta=29.2^\circ$
C2	5 \times 5 \times 0.5 mm Beta-Barium Borate (BBO) Crystal, cut [‡] at $\theta=38^\circ$
RF1-RF2	Newport Gold-coated retro-reflector
L1	Focal length 5 cm
L2-L3	Focal length 10 cm
L4	Focal length 15 cm
L5	Focal length 7.5 cm, 250-430 nm, AR coated
L6	Focal length 7.5 cm, 250-430 nm, AR coated
PM	GSI-Lumonics Inc. Gold Coated Aluminum, 90° off Axis Parabolic Mirror 2.875 cm Focal length
BS1	50/50 beam splitter
F1	Newport UG11 filter or Schott DUG11X filter

[†] Refer to Figure 2.3 for definition of cut angle.

[‡] Refer to Figure 2.3 for definition of cut angle.

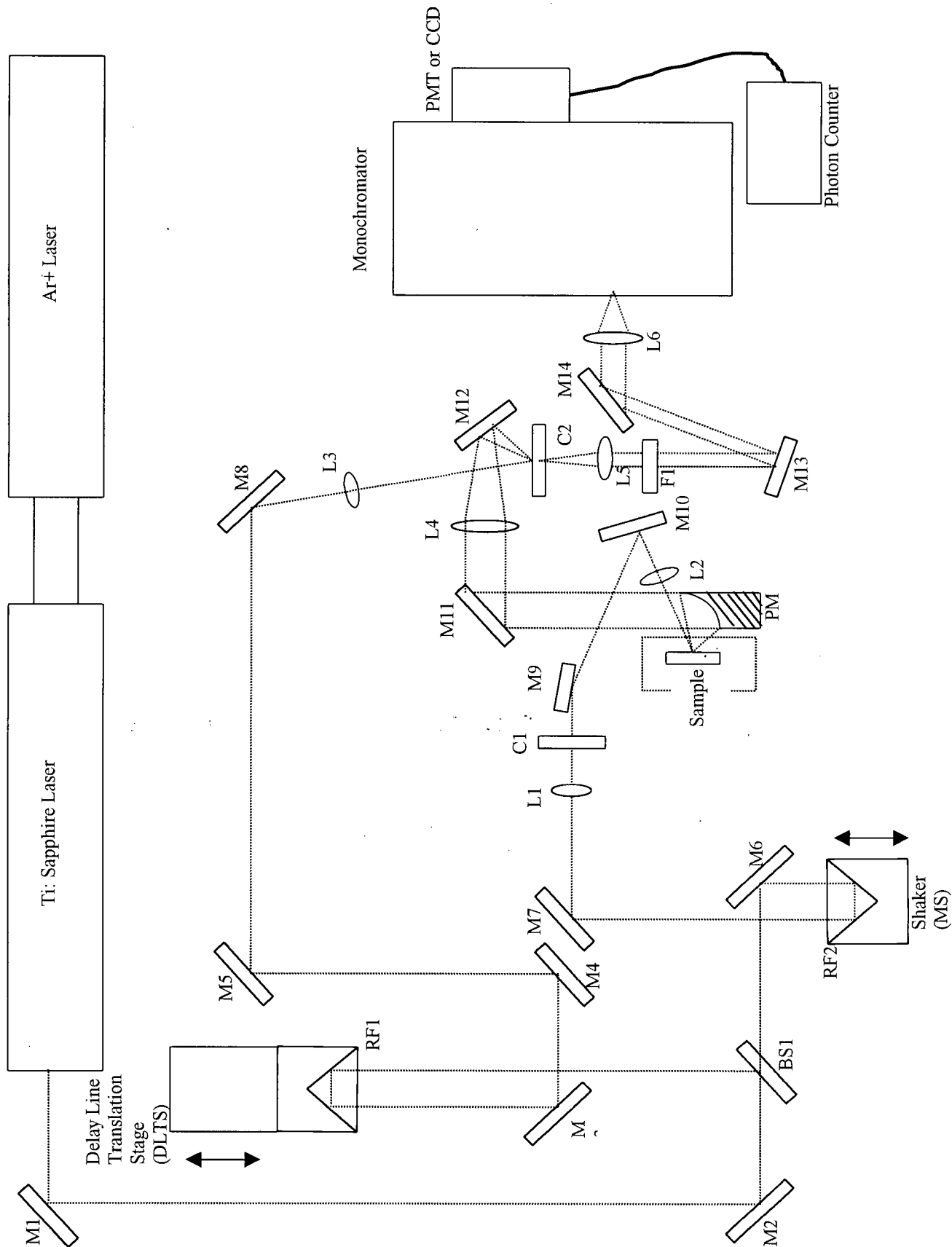


Figure 3.1: Schematic set-up for femto-second time resolved photoluminescence spectroscopy.

3.2 Major Challenges and Solutions

The previous setup used in Reference [18] had a sufficient signal to noise ratio to time-resolve the transient PL emitted by bulk PPV. The PL strength of the signal from samples studied in this work was considerably less than that of bulk PPV. Several changes were made to increase the system sensitivity by a factor of approximately three times. Details of these improvements are described in this section.

3.2.1 General Alignment

Proper alignment of all components is critical to achieving high sensitivity in this complex optical setup. The first phase of the procedure involves ensuring that all beam paths lie in a common plane parallel to the optical table, and that all focusing optics are aligned precisely on the optical axis of the beam passing through them.

3.2.2 Gate and PL Spot walk-off on Upconversion Crystal

Usually, during an upconversion experiment, the nonlinear crystal C2 needs to be rotated to maximize the signal at different wavelengths. The focused gate and PL spots on the crystal must not “walk off” each other as the crystal is rotated. Gate and PL beams must therefore be focused right on the rotation axis of the rotation stage. To achieve this, first rotate crystal C2 so that the gate beam is perpendicular to the surface of the crystal. Second, translate crystal C2 in the x direction, so that the spot is focused on the Teflon and imaged by the CCD camera. Mark the position of spot on the screen. Now rotate crystal C2 and adjust the x or y positions of the crystal until the gate spot does not walk when crystal C2 is rotated. Finally,

adjust the position and focus of the PL beam so that it overlaps with the gate spot on the rotation stage axis.

3.2.3 Shape of Excitation Spot

The UV excitation beam is generated by focusing the IR laser beam onto the non-linear crystal C1. In order to make sure the shape of the excitation spot on the sample is a circle for optimum overlap with the gate beam, the Beta-Barium Borate (BBO) crystal is cut at an angle of 29.2° to the optic axis. Such a cut angle allows normal incidence second harmonic generation with ~ 800 nm laser pulses, which minimizes the distortion in the second harmonic generation beam.

3.2.4 Nonlinear crystal for upconversion

A negative uniaxial crystal (BBO, $n_e < n_o$) was used for upconversion. For optimum results, the crystal needs to be cut properly so that it can upconvert a wide frequency range of the PL spectrum. In our upconversion experiment, the BBO crystal is cut at 38° . With such a cut angle, this BBO crystal can be used to upconvert PL wavelengths ranging from the visible (500 nm) to the IR (1200 nm), when used in combination with gate wavelengths from 745 nm-800 nm. The polar plot in Figure 3.2 gives the phase matching angle as a function of the PL wavelength for a 798 nm gate pulse (thick solid curve) as obtained using the code in Appendix A. The angle between the gate and PL beams is taken to be 20° . Less than 30° of rotation of the crystal can cover the PL wavelength range of 500 nm-1200 nm.

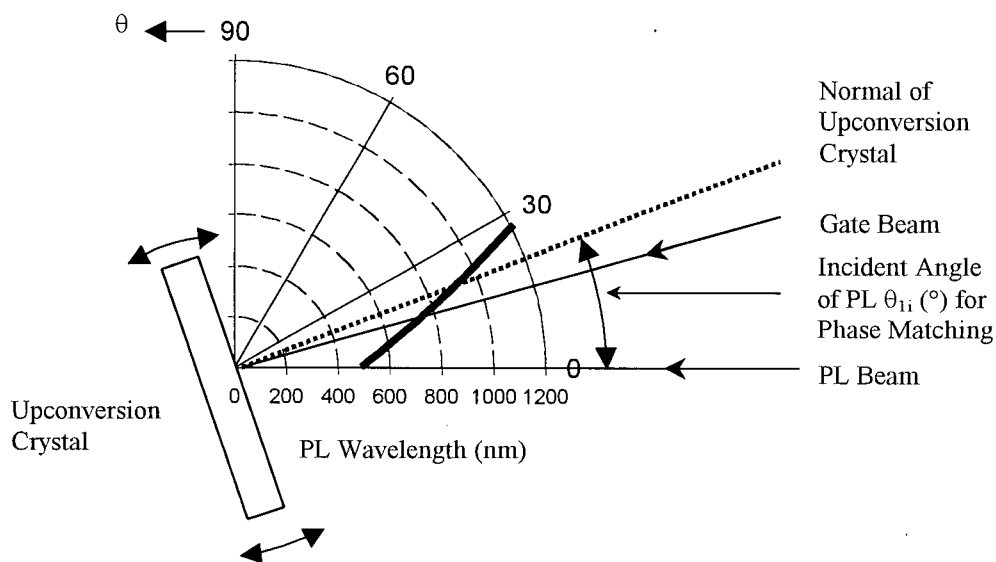


Figure 3.2: Polar plot of the phase matching angle as a function of the PL wavelength (thick solid curve). Wavelength of the gate was 798 nm. The external angle between the gate and the PL beams was 20°.

3.2.5 Gate and PL beam geometry

To measure the angle between the gate and the PL, the most accurate method is to determine the angles at which the crystal surface reflects the gate and the PL beams back on themselves, using the Labview program *rotate.vi* to rotate the crystal and using *MM2000TellPosition.vi* to indicate the position of the crystal. This method is more straightforward and quicker than that described in Reference [18] which was based on second harmonic generation from the gate and the reflected laser beam from the sample surface.

The PL spectra of the organic semiconductors studied in this work are 150 nm -200 nm wide (taking MEH-PPV as an example, the range is 550 nm - 700 nm). For an angle of 18° between the gate and the PL beams, the angular difference between the sum frequency

propagation and the gate propagation under phase matching condition is plotted as a function of the PL wavelengths in Figure 3.3. The direction of sum frequency propagation only varies by $\sim 1^\circ$ for PL wavelengths between 550 nm to 700 nm. Thus, once the collection optics (M13/M14/L6) are well aligned for upconversion of one PL wavelength, even though the crystal C2 is rotated for upconverting different parts (wavelengths) of the photoluminescence spectra, the adjustment of the collection optics is minor. We just need to rotate the crystal C2 to the right angle (calculated by the Maple code listed in Appendix A), position the monochromator to the right wavelength, and set the delay line translation stage to ~ 3 picosecond delay. A very minor adjustment of M13/M14 then results in an optimized upconverted signal for the next PL wavelength. The same principal applies to other polymer samples which have a similar PL bandwidth.

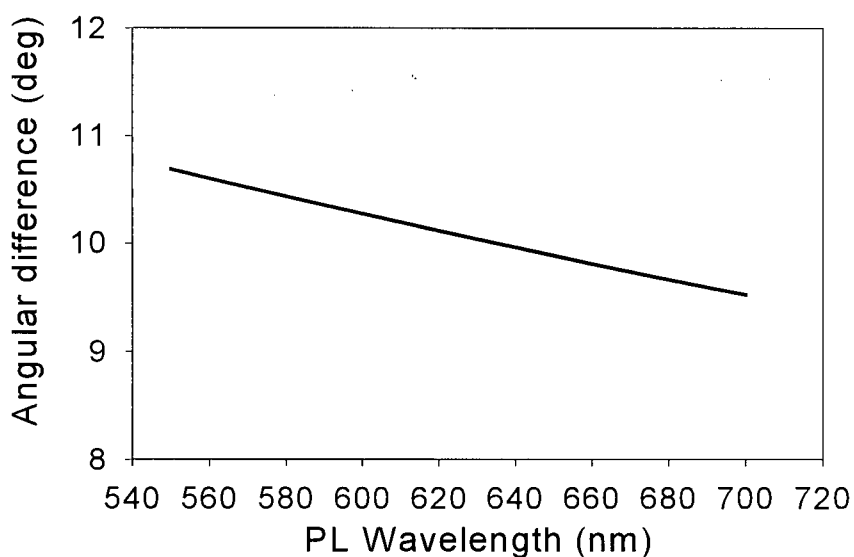


Figure 3.3: The angular difference between the sum frequency propagation and the gate propagation as a function of PL wavelength under phase matched conditions. The wavelength of the gate was 798 nm, and the external angle between the gate and the PL was 18° .

3.2.6 PMT Dark Current

The dark count rate of the detector directly impacts the achievable signal-to-noise-ratio (SNR). The PMT dark count rate is sensitive to the ambient temperature and internal heating effects. Practice has shown that if the room temperature is kept stable below 18° and the PMT is turned on immediately before the time-resolved experiment, the dark count rate starts at only 2-5 counts per second, and increases slowly to around 10 counts per second within three hours. A typical run involves acquiring signal counts in 20 second integrations for each of ~70 different delays, where the background dark counts over the same 20 seconds are monitored every five delay points. Between each run at fixed wavelength, the PMT is turned off and a fan is used to cool the PMT before the next run.

3.2.7 LN/CCD as a Detector for Extremely Weak Signals

Although much effort has been implemented to reduce the background count rate of the PMT, it is still not low enough to obtain a good signal to noise ratio from some of the weaker sources studied here, which yield peak signals of ≤ 3 counts per second. To overcome this problem, a liquid nitrogen cooled CCD detector from Princeton Instruments Inc. (Model: Spec10:100BR) was used in place of the PMT as a detector when the upconverted signal was very weak. The CCD detector is MgF1 coated for broad-band operation in the 200 nm - 1100 nm range. Liquid nitrogen was used to cool the detector, so that it effectively has zero dark counts. The detector consists of a 1340×100 array of pixels and is specifically designed for spectroscopy measurements. The size of each pixel is $20 \times 20 \mu\text{m}$.

To use the detector in upconversion experiments, we want to integrate every photon that reaches the detector. 35,000 (350×100) pixels are therefore combined to form a “super pixel” by setting an appropriate region of interest (ROI) in the CCD control software [27]. To correctly set the ROI, the monochromator is positioned to the peak wavelength of the SHG of gate, and the monochromator output is imaged on the full CCD chip. M13/M14 are adjusted so that the image on the CCD chip is sharp and strong (typically over 1000 counts per second). As the upconverted signal and the SHG originate from the same spot on the nonlinear crystal and pass through the same optics, they should be imaged at the same position on the CCD chip. Considering the wavelength difference between SHG and upconverted signal and the chromatic aberration of the optics, a ROI which is larger than the SHG image is set to make sure the region can detect every photon of the signal. In our experiment, a 350×100 rectangular ROI was centered on the SHG image.

A complication arises due to the relatively large IR response of the CCD detector as compared to the PMT. To isolate the detector from any unwanted light in the lab, three layers of black electrical tape were used to seal the gap between the CCD window and the wall of the monochromator. All the edges of the monochromator were also sealed with black electrical tape. The height of the entrance slit of the monochromator is narrowed down to ~ 2 mm by black electrical tape. Several pieces of black cardboard were used to shield the PL, scattered gate beam and the light from the computer monitor from entering the entrance slit of the monochromator. Most importantly, a DUG11X filter from Schott Glass Technology Inc. was used in place of the UG11 filter to filter out the strong IR background of the gate. The

DUG11X is a UG11 filter with a special coating, which only has one transmission window in the 250 nm - 400 nm range.

The CCD detector is equipped with a shutter in front of the chip to control photon integration time. For the above mentioned 350×100 ROI, the pure dark count rate with the shutter totally closed is $385 \pm 10/30$ sec. With the DUG11X filter inserted in place of the UG11 filter and with the pure dark count rate ($385 \pm 10/30$ sec) subtracted by the control software [27], the gate beam background is below $100/30$ sec while the net upconverted signal is in the range of 50-250/30 sec, depending on the wavelength being upconverted and the delay. Data acquisition with the CCD detector is performed in Mode I described in Section 3.3.5. A typical run consisting of 30-40 delays and a 30 second integration time per delay takes about one hour. Occasionally, the integration is corrupted by high intensity spikes due to cosmic rays.

3.3 Upconversion Data Acquisition

3.3.1 The zero delay point: Laser upconversion

After all the optical components preceding crystal C2 are properly aligned, the next step is to determine the position of the delay translation stage (DLTS) that corresponds to zero time delay. The laser beam is split at BS1 into gate and excitation beams. The excitation beam hits the sample before being focused onto the upconversion crystal, C2. It is not practical to measure and set the two path lengths to be closer than ~ 3 cm. Therefore, laser upconversion is used to determine the exact zero delay point.

Referring back to Figure 3.1, the frequency doubling crystal C1 and focusing lens L1 are removed from the excitation beam path. The sample in the cryostat is lifted slightly so that the laser is focused on the Teflon below the sample. The scattered laser beam is then focused on C2 in the same manner as the PL. After the scattered spot and gate spot are overlapped on crystal C2 and the crystal is rotated to the right angle for laser upconversion, a lens with a focal length of ~ 200 mm focuses the non-phase-matched second harmonic generated from the gate onto a Si-detector. As the laser upconversion signal is generated at the same point in the crystal, and is the same wavelength as the SHG of the gate pulses, the scattered laser upconversion signal will also be focused on the Si-detector when it is available. The Si-detector is AC coupled to an oscilloscope, and the mini-shaker MS is turned on. The delay line translation stage DLTS is slowly moved, and as the translation stage passes through the zero delay point, a number of spikes appear on the oscilloscope screen. The spikes appear in pairs, one of each pair represents the forward and backward pass of the shaker through the zero delay point. To find exactly the zero delay point, the delay translation stage is moved so all the spikes are evenly spaced on the oscilloscope screen. If the mini-shaker is then turned off and the Si-detector is DC coupled into the oscilloscope, the upconverted signal appears as a DC level. A combination of fine tweaking of the delay line and M12, and fine rotations (in 0.1° increments) of crystal C2 can result in a scattered laser upconverted signal close to 1 volt. This scattered laser upconverted signal is visible to the eye on florescent paper and is a valuable tool for aligning the collection optics, the monochromator, and for positioning the PMT.

The zero delay point determined from the scattered laser upconversion is not exactly the same as that for the actual PL upconversion, after the frequency doubling crystal C1 and

L1 are re-inserted. Experience has shown that they are within 5 mm apart on the delay line translation stage. The real zero delay point of the actual PL upconversion is determined after the PL upconversion signal is observed. Details of this are discussed in section 3.3.4.

3.3.2 Alignment of Collection Optics

The collection optics consists of M13, M14 and L6. M13 and M14 are 2 inch diameter UV mirrors. L6 is a UV lens mounted on a 3-D translation stage. Positioning L6 is particularly important. The laser upconversion signal (LUS) is used to align the collection optics, including M13/M14 and the PMT. This is preferred over using the second harmonic generation (SHG) of the gate alone, as the LUS is a dot while the SHG of the gate is ring shaped. Firstly, the entrance and middle slits of the monochromator are opened to 2000 μm , and the lid of the monochromator and the focus lens L6 are removed. The LUS is collimated by L5, reflected by M13/M14 to the entrance slit of the monochromator. By tweaking M13/M14, the LUS is aligned to be parallel to the optical stage and perpendicular to the entrance slit of the monochromator. After positioning the monochromator to the peak wavelength of the LUS, adjust the UV mirror and the UV lens inside the monochromator for maximum signal on PMT[§]. Finally, replace the lid, and adjust L6 for maximum signal on the PMT. Normally, 3-5 million counts per second can be achieved from the LUS.

[§] The second grating of the monochromator was bypassed by placing a UV mirror and lens after the middle slit, for the reasons described in Reference [18]. The signal is directed to the detector through a hole in the side of the lid.

3.3.3 Maximizing the Intensity of PL

The nonlinear crystal C1 and lens L1 are re-inserted for the PL upconversion experiment. The intensity of the PL should be maximized before being upconverted.

The PL excited by UV pulses is collimated by the parabolic mirror (PM), reflected by M11/M12 and focused by L4 onto crystal C2. C2 is translated so that the PL focused on the Teflon tape is imaged by the CCD camera. A combination of tweaking L2 and L4 and moving the sample up and down results in a tightly focused, bright and round spot on the screen.

3.3.4 The Sum Frequency Signal

To obtain good overlap of the PL and the gate beams on crystal C2, neutral density filters should be inserted into the gate path to reduce the intensity of the gate spot being imaged. When the attenuated gate and maximized PL spots are overlapped on the surface of the Teflon tape using the CCD camera, their respective diameters on the monitor should be ~ 1 cm and ~ 0.5 cm. C2 is then translated back and the neutral density filters are removed so that the PL and gate beams are focused on the surface of the nonlinear crystal.

The geometry of the gate, the PL and the crystal C2 was described in section 3.2.5. C2 is rotated to the phase matching angle for the wavelength of interest, as calculated by the Maple code (Appendix A). The delay line translation stage (DLTS) is set to approximately +5 ps delay from the zero delay point determined by laser upconversion. Next, the monochromator is positioned to the peak wavelength of the SHG from the gate alone and the PMT signal is maximized by adjusting M13/M14. Then the monochromator is set to the wavelength corresponding to the desired upconverted signal. The wavelength of the

upconverted signal for MEH-PPV PL (550 nm - 700 nm) with an 800 nm gate is in the range of 325-370 nm. As the upconverted signal is much weaker than both the SHG and the PL background, a Newport UG11 filter that has a transmission window between 250 nm and 400 nm is inserted between M13 and L5 to filter both of them. Most likely, a small signal should be observed. If not, adjust the delay line. Once a small signal is available, a combination of adjusting M13/M14, rotating C2, and adjusting M12 for better gate/PL overlap results in an optimized upconverted signal. The zero delay point of the upconverted signal of the PL is approximately determined by moving the DLTS towards the “negative delay” direction until the upconverted signal suddenly becomes equal to the background. The precise zero delay point position is not determined, and is not crucial for interpreting the data obtained to this point.

3.3.5 Data Collection

Two modes of data collection were used. Mode I consists of fixing the monochromator and varying the delay. Mode II involves scanning the monochromator at a given delay.

For Mode I, with a high signal-to-noise ratio, the PMT counts were monitored in 20 second bins for each delay. The dark count rate of the PMT is controlled to be as low as possible using the method described in section 3.2.5. The PMT dark count background was recorded every five data points by blocking the excitation beam. The temperature of the sample is controlled within 0.1K. The best temperature stability was achieved when the liquid nitrogen level was above the bottom of the sample holder but well below the sample itself. A typical run consisting of 60-70 data points takes about one hour.

For Mode II, the upconverted spectrum is scanned at given delays with a step-size of 0.5 nm. At the shorter delays (<30 ps), the more intensive spectra were scanned at 1 second/point. At longer delays (50-200 ps), the weaker spectra was scanned at 2 second/point. Each spectrum consists of 80 data points.

3.3.6 White light upconversion

The spectra taken at fixed delay (Mode II) require calibration if they are to be quantitatively analyzed. The reason that more than a single frequency can be upconverted for a given crystal orientation has partly to do with the large cone angle ($\sim 10^\circ$) with which the PL signal is focused onto the upconversion crystal. The PL in fact is not incident at a single angle, but over a range of angles, and so different frequency components of the PL spectrum are simultaneously phase-matched. There is also a finite extent of $\sim \pm 1.5^\circ$ to the phase-matching range for a given frequency at a fixed angle of incidence.

In principal, the system could be calibrated by replacing the PL source with a diffuse, broadband white light source. This proved to be difficult to achieve without removing the entire cryostat. Instead, to perform white light upconversion, as shown in Figure 3.4, the white light of a 100W tungsten quartz halogen bulb (equivalent to a 3200 K blackbody, Model Oriel 77501) was coupled into an Ocean Optics Inc. fiber (model: P600-2-VIS/NIR) with a facet diameter of 100 μm . The light output from the fiber was collimated by a lens L_w (focal length 25 mm) and then focused by L_4 onto the nonlinear crystal, in the same manner as the PL was focused. The main difference between this and the PL source was the f-number of L_4 imaged on the crystal. In the PL setup, it was $\sim f4$, while in the white light setup it was $\sim f8$. All other

conditions such as the wavelength of the gate beam, angle between the gate beam and the PL beam (now the white light beam), collection optics and insertion of the UG11 filter were unchanged from the PL upconversion setup. The spectra of upconverted photons are measured in Mode II. As the spectrum of polymer PL is in the visible range, a Newport GG.455 filter was inserted in the tungsten lamp light path to cut off wavelengths shorter than 455 nm, in order to eliminate strong white light background in the sum frequency beam. The spectral response curves were taken at different phase-matching angles, as presented in Chapter 4.

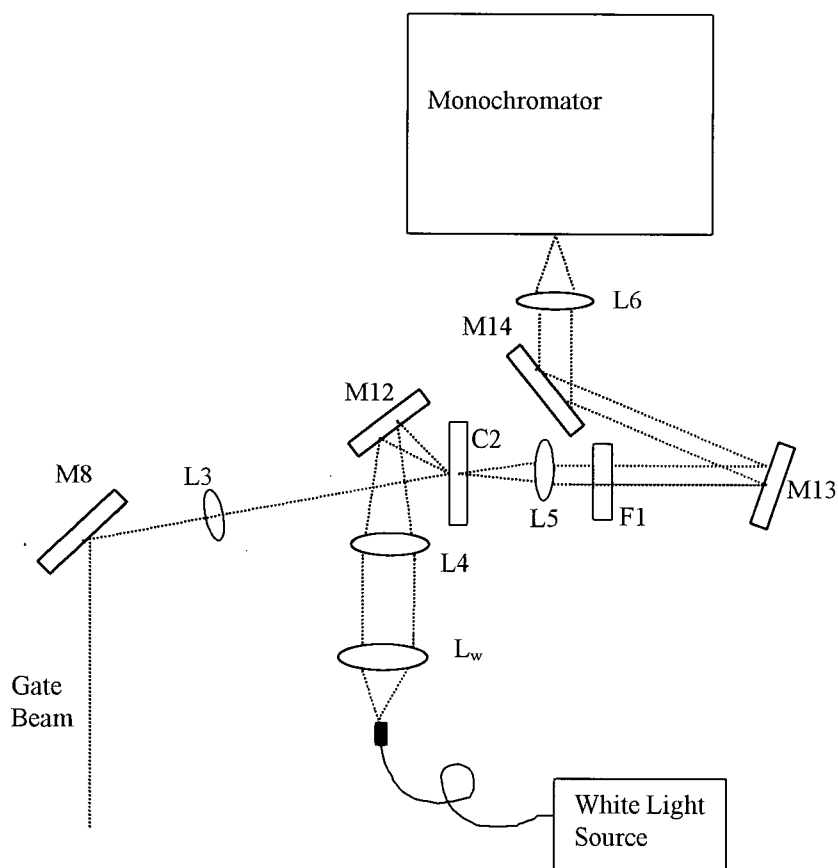


Figure 3.4: Schematic Setup for White Light Upconversion.

3.4 Sample preparation

In this thesis, two types of PPV derivatives, MEH-PPV and DP-PPV are studied. They were prepared in three forms.

1. Bulk film on microscope slide glass;
2. Encapsulated in anodized alumina on aluminum foil;
3. Encapsulated in commercially anodized disks (Anodisc 13) from Whatman Inc.;[28]
4. Encapsulated in silanized Anodisc material.

All the samples described below were prepared by members of Dr. M.O.Wolf's group in the Department of Chemistry, University of British Columbia, Canada.

3.4.1 Bulk Samples: Film on microscope-slides

1. MEH-PPV

MEH-PPV films were synthesized using the method described in Reference [19]. A 0.6% by weight solution of MEH-PPV in THF (Tetrahydrofuran) was spin-coated onto microscope slides. The chemical reaction route used to prepare the MEH-PPV is illustrated in Figure 3.5.

2. DP-PPV

DP-PPV films were synthesized following a chlorine precursor process described in the literature [22]. First, a soluble chlorine precursor polymer was synthesized and dissolved in toluene. 0.03% by weight prepolymer in toluene was spin-coated onto microscope slides. After drying in vacuum, the sample was heated to 280°C for 2 hours. The chemical reaction route used to prepare the polymer is illustrated in Figure 3.6.

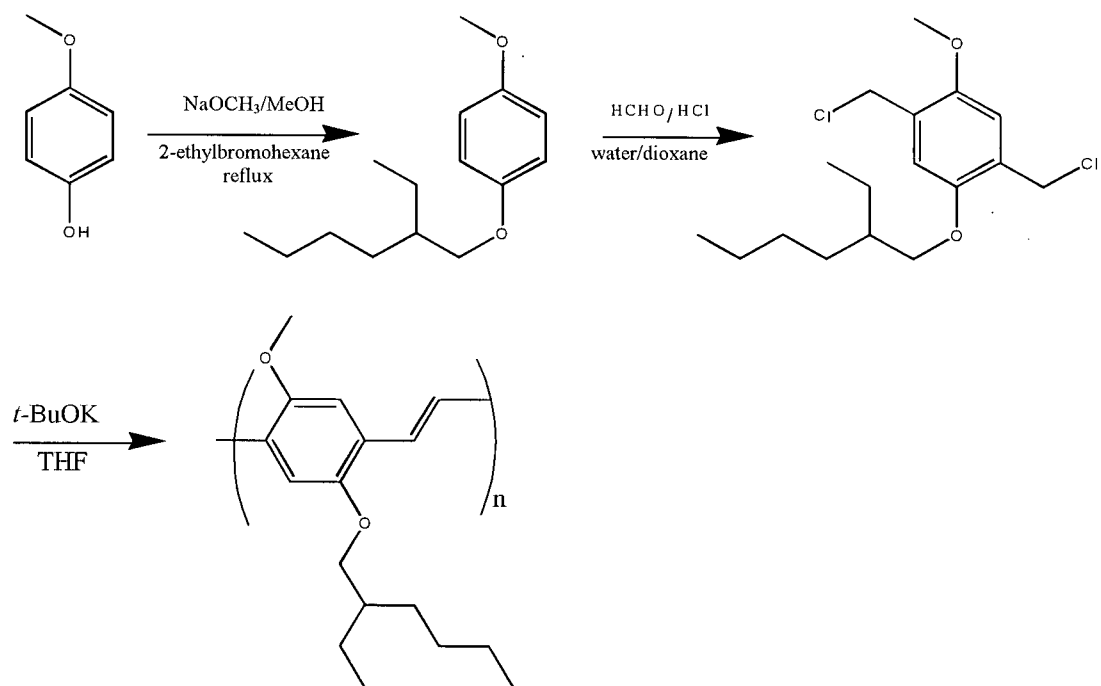


Figure3.5: Synthesis of MEH-PPV.

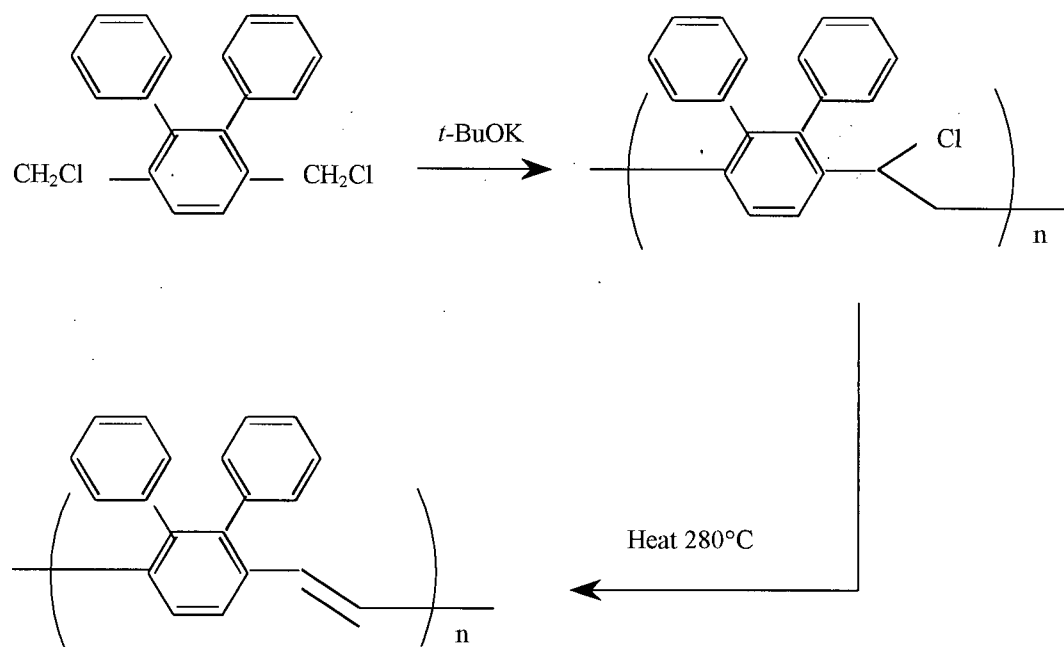


Figure3.6: Synthesis of DP-PPV.

3.4.2 Host Material Preparation

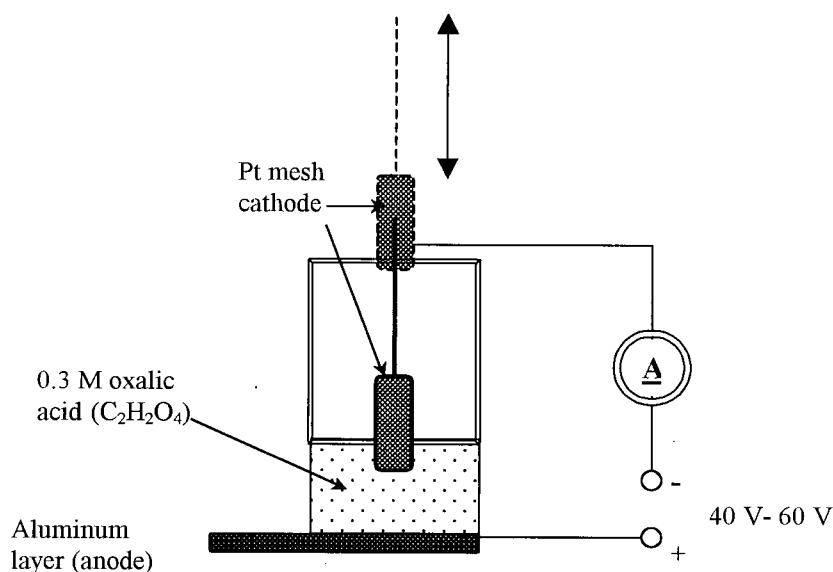


Figure3.7: Set-up for Anodization of Aluminum.

1. Anodized Alumina on Aluminum Foil

Anodization is a process in which an aluminum layer is oxidized electrochemically. Under certain conditions, self-organized nanopore structures are formed in the aluminumoxide (alumina) layer [20].

The aluminum foil, which is 0.13 mm thick with a purity of 99.99%, is first degreased with acetone, then it is anodized with 0.3 M oxalic acid ($C_2H_2O_4$) as electrolyte, with an applied voltage of 40-60 V. The anodization is complete once the current starts dropping from its steady value. This process normally takes about one hour. The sample is rinsed with distilled water. The pores are then widened by dipping the oxidized aluminum layer into 5% phosphoric acid (H_3PO_4) for 45 minutes. A thin aluminum layer sometimes remains at the bottom of the alumina matrix. Figure 3.7 gives a schematic setup for the anodizing process.

Figure 3.8 gives a schematic diagram of the aluminum sample before and after the anodization process. Figure 3.9 gives SEM pictures of anodized alumina on aluminum foil with both top and cross sectional views. The diameter of the pores varies between 50-90 nm across the sample. The pores are self-organized with a roughly hexagonal order but they are not uniform across the whole sample. The depth of the pores of the anodized alumina is approximately $10\ \mu\text{m}$.

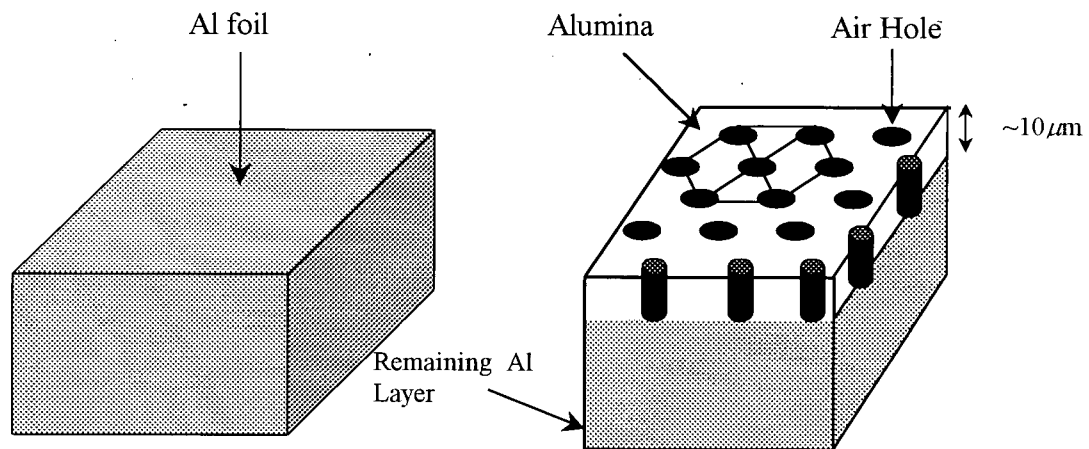


Figure 3.8: Schematic graph of sample before (a) and after (b) anodizing.

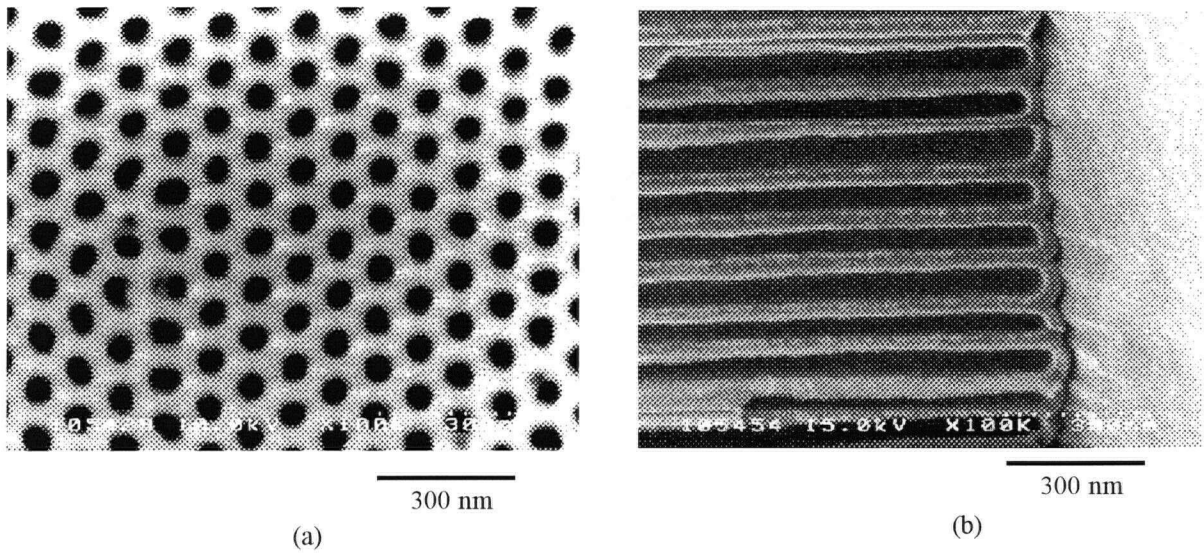


Figure 3.9: SEM pictures of anodized alumina on aluminum foil.
(a) Top view and (b) cross sectional view. (Images obtained by Keri Kwong)

2. Anodisc 13 membranes from Whatman Inc.

Anodisc 13 membranes, manufactured by Whatman Inc., consist of a thin wafer of

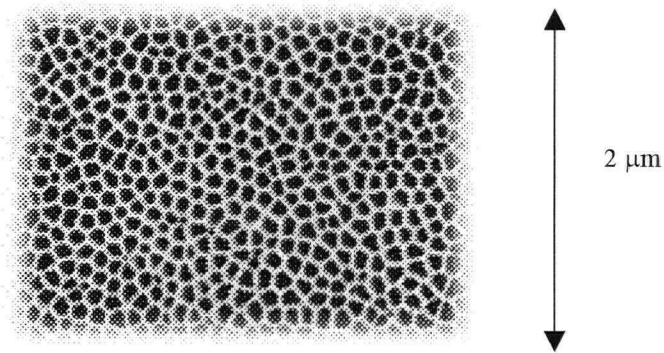


Figure 3.10: Pores of Anodisc [28].

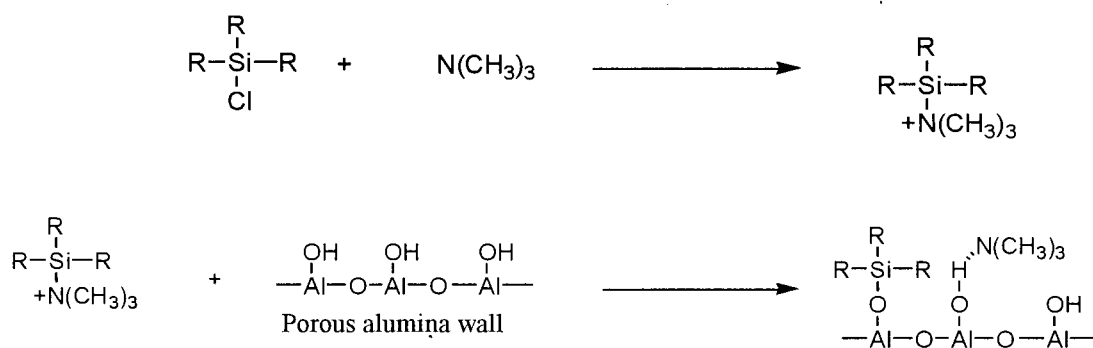
porous alumina, which can be used as a host to light emitting materials. These porous membranes have an asymmetric structure [35]. The majority of the membrane is comprised of pores with 200 nm pore diameters with a $\sim 60 \mu\text{m}$ depth. The other side of the membrane contains ~ 20 nm pore diameters with a $2 \mu\text{m}$ depth. Figure 3.10 shows the pores in the anodisc membrane [28]. More information about this material can be found in References [28] [35].

2. Silanization of Anodisc

Silanization is a chemical process used to modify the internal walls of porous materials, such as alumina or silica. This process allows the interior of the pores to be modified with alkyl groups, as shown in Figure 3.11, before the polymer chains are encapsulated. The purpose of silanization of porous materials is to help encapsulate more polymers into the pores by modifying the interaction of the polymer chain with the silanized pore walls. In principal, the silanization process also offers better protection to the encapsulated polymer chains because

the oxygen in the alumina, which is believed to be involved in the degradation of the polymer, is screened from the polymer chain by silanization [34] [23]. Some of the Anodisc membranes were silanized with Me_3SiCl (trimethylchlorosilane). Full details are described in Appendix C. Figure 3.11 shows the chemical reaction route used for the silanization. Triethylamine ($\text{N}(\text{CH}_3)_3$) is used as a catalyst which reacts first with the silane and then reacts with the alumina.

In this thesis, the Anodisc used to host DP-PPV was silanized, while the Anodisc used to host MEH-PPV was not silanized.



Note: R= Methyl (TMS)

Figure 3.11: Chemical reaction route for silanization of Anodisc.

3.4.3 Encapsulating MEH-PPV into anodized Alumina or Anodisc

To encapsulate MEH-PPV into the host materials described in section 3.4.2, the host material is immersed in a 0.025wt% MEH-PPV THF solution for two days in the dark, under nitrogen atmosphere to avoid photodegradation. The sample is then rinsed with distilled water, dried and stored in a sealed bottle filled with nitrogen.

3.4.4 Encapsulating DP-PPV into anodized Alumina or Anodisc

As DP-PPV is not soluble in THF, a soluble DP-PPV prepolymer was synthesized as described in section 3.4.1. The host material is immersed in 0.03% by weight DP-PPV prepolymer toluene solution for two days in the dark, nitrogen atmosphere to avoid photo degradation. The sample was then rinsed with distilled water, dried in vacuum and heated to 280°C for 2 hours to convert the prepolymer to DP-PPV.

Chapter 4

Experimental Results

Table 4.1 summarizes the properties of the MEH-PPV and DP-PPV samples and their labels used in this work. Methods of preparing these samples were described in Section 3.4. In the rest of this thesis, bulk MEH-PPV or bulk DP-PPV refers to the polymer on microscopic slides, Anodisc MEH-PPV or Anodisc DP-PPV refers to the polymer encapsulated in the Anodisc 13 membranes from Whatman Inc., and Anodized MEH-PPV or Anodized DP-PPV refers to the polymer encapsulated in the anodized alumina made by members of Dr. M.O.Wolf's group in UBC.

Table 4.1 Sample Properties and Sample Labels

Properties \ Sample Labels	Bulk MEH-PPV	Anodized MEH-PPV	Anodisc MEH-PPV	Bulk DP-PPV	Anodized DP-PPV	Anodisc DP-PPV
Polymer Type	MEH-PPV	MEH-PPV	MEH-PPV	DP-PPV	DP-PPV	DP-PPV
Host Type	Glass Slide	Anodized Alumina on Aluminum Foil	Anodisc 13 (Whatman Inc.)	Glass Slide	Anodized Alumina on Aluminum Foil	Anodisc 13 (Whatman Inc.)
Host	Flat	50-90 nm diameter pores, 10 μm thick	Side 1: ~200 nm diameter pores, ~60 μm thick Side 2: ~20 nm diameter pores, ~2 μm thick	Flat	50-90 nm diameter pores, 10 μm thick	Side 1: ~200 nm diameter pores, ~60 μm thick Side 2: ~20 nm diameter pores, ~2 μm thick
Silanized?	-	No	No	-	No	Yes
Note: Anodized samples and anodisc samples are both referred to as "nanostructured samples".						

4.1 Time-integrated Spectra

4.1.1. Effects of Nanoporous Hosts

The time-integrated photoluminescence spectra for bulk MEH-PPV and bulk DP-PPV at 77 K are plotted in Figure 4.1. Their shape is quite similar to the published [16] spectra from other conjugated polymers such as PPV. Referring to Section 2.2, in each of the spectra, the large peaks at the highest energies (2.05 eV for MEH-PPV and 2.45 eV for DP-PPV) result from a purely electronic transition from the bottom of the first excited state S_1 to the bottom of the ground state S_0 (the $S_{0,0}$ or the 0-phonon transition). The less intensive peaks at lower energies (1.90 eV for MEH-PPV and 2.30 eV for DP-PPV) are attributed to a one-phonon assisted transition from the bottom of S_1 to the first vibrational state in S_0 , and are

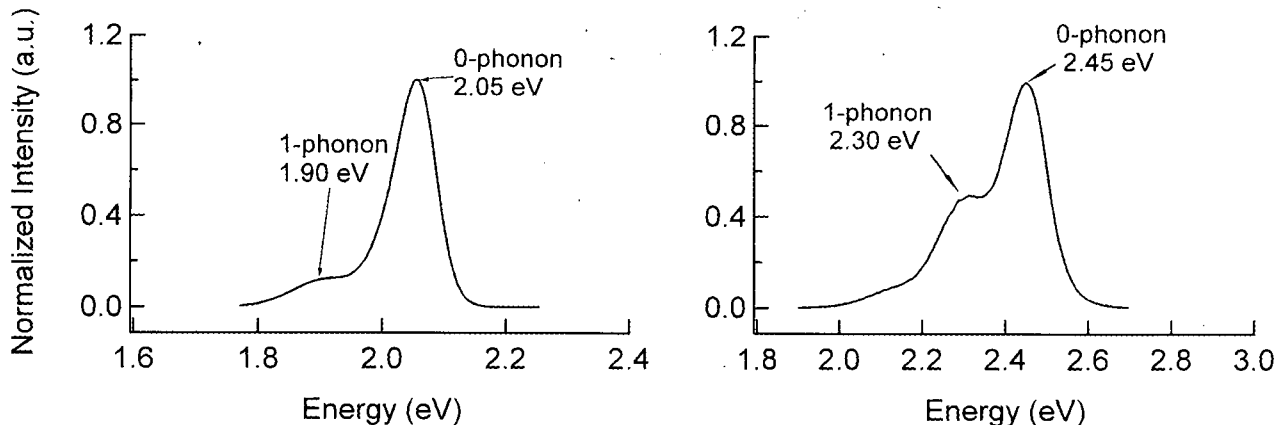


Figure 4.1: Photoluminescence Spectra of (a) bulk MEH-PPV and (b) bulk DP-PPV at 77 K. Excitation wavelength was 398 nm.

referred to as the $S_{0,1}$ or the 1-phonon transitions. The less obvious little “bump” near 2.11 eV for DP-PPV is attributed to a two-phonon assisted transition and is referred to as the $S_{0,2}$ or the 2-phonon transition. For bulk MEH-PPV, the $S_{0,2}$ or 2-phonon transition was not observed. The broad peaks reflect the inhomogeneously broadened density of states (DOS) due to the distribution of effective conjugation lengths (ECL) in the polymer chains.

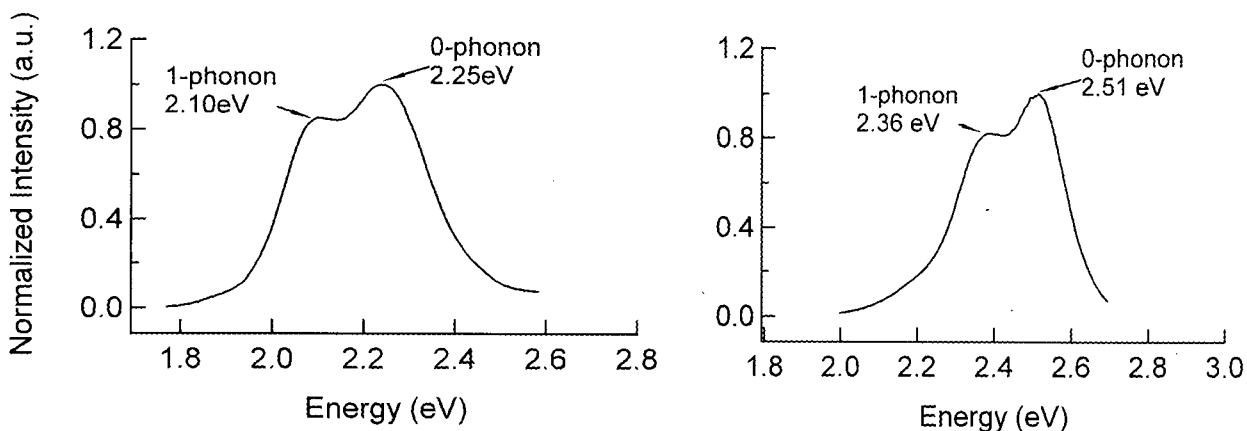


Figure 4.2: Photoluminescence Spectra of (a) Anodisc MEH-PPV and (b) Anodisc DP-PPV at 77 K. Excitation wavelength was 398 nm.

The time-integrated photoluminescence spectra of Anodisc MEH-PPV and Anodisc DP-PPV at 77 K are plotted in Figure 4.2. The encapsulation clearly results in a significant effect of the on the shape and energies of the spectra.

In order to quantitatively analyze these spectra, multiple Gaussian functions are used to fit the time-integrated spectra of bulk and Anodisc samples for MEH-PPV and DP-PPV. In all cases considered, two-Gaussian functions do not yield as good fits as those obtained with three-Gaussians. With 3-Gaussians, two of the three (labeled 1 and 2) always have similar line widths and are separated by the expected phonon energy, while the third has a different line width and energy.

For direct comparison, the normalized PL spectra of MEH-PPV and DP-PPV at 77 K for both bulk and nanostructured samples are plotted in Figure 4.5. One can observe that there is a significant blue-shift for the PL of the nanostructured samples, ranging from 0.034 – 0.183 eV. A similar blue-shift (approximately 0.15 eV) was also observed by Zojer *et al.* on PPV chains isolated in a self-assembled lyotropic liquid crystal host [24,25]. In the nanostructured

samples, the amount of blue-shift of MEH-PPV is greater than that of DP-PPV. For the same guest polymer, the Anodisc samples result in a greater blue shift than the Anodized samples.

The relative (with respect to the 0-0 transition peak) intensity of the 0-1 transition peak increases in the nanostructured samples compared to the bulk samples. Similar results were also observed by Zojor on isolated PPV polymer chain [25].

In addition, it is observed that the spectra of the nanostructured samples become wider, indicating a greater degree of inhomogeneous broadening of the ECL energy density of states. Similar results were also observed by Zojor on isolated PPV polymer chain [25].

Table 4.2 summarizes the observed blue shifts and the broadening of the 0-0 transition peaks, the relative amplitude of the 0-1 peak with respect to the 0-0 peak, and the blue shift of the third Gaussian for both MEH-PPV and DP-PPV in different host materials.

Table 4.2 Comparison of Spectra of Bulk and Nanostructured MEH-PPV and DP-PPV

Sample Label	Blueshift of 0-0 peak	Broadening of 0-0 peak	$\frac{\text{Amplitude 1-0}}{\text{Amplitude 0-0}}$	Blueshift of third Gaussian	Broadening of third Gaussian
Anodized MEH-PPV	+0.058 eV	-	-	-	-
Anodisc MEH-PPV	+0.183 eV	+100%	81%	0.163 eV	+115%
Anodized DP-PPV	+0.034 eV	-	-	-	-
Anodisc DP-PPV	+0.068 eV	+35%	58%	0.101 eV	+10%
Bulk MEH-PPV	-	-	25%	-	-
Bulk DP-PPV	-	-	35%	-	-

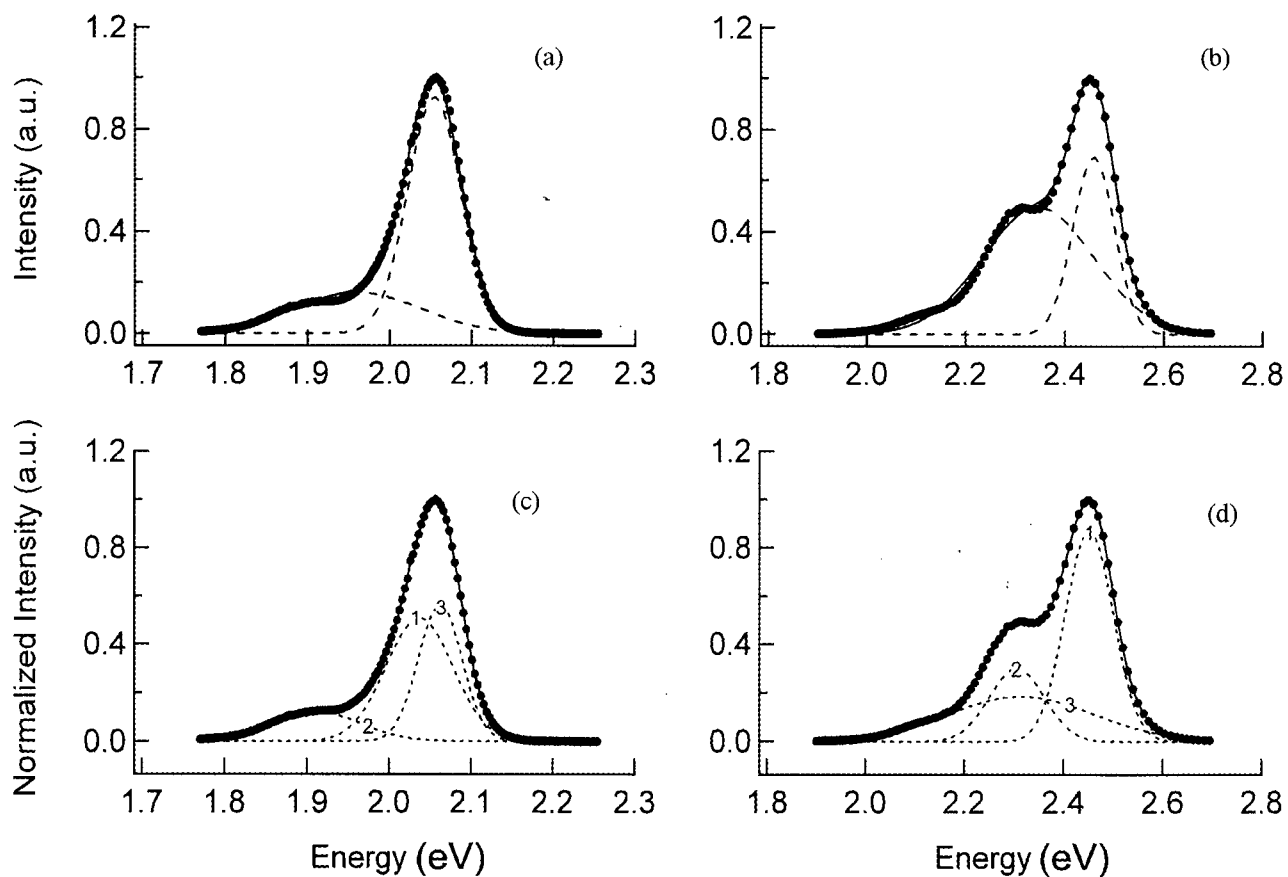


Figure 4.3: Two-Gaussian fits for (a) bulk MEH-PPV and (b) bulk DP-PPV PL at 77 K and three-Gaussian fits for (c) bulk MEH-PPV and (d) bulk DP-PPV PL at 77 K. In all cases, the dashed lines show the individual Gaussians, and the solid lines show the sum of the Gaussians.

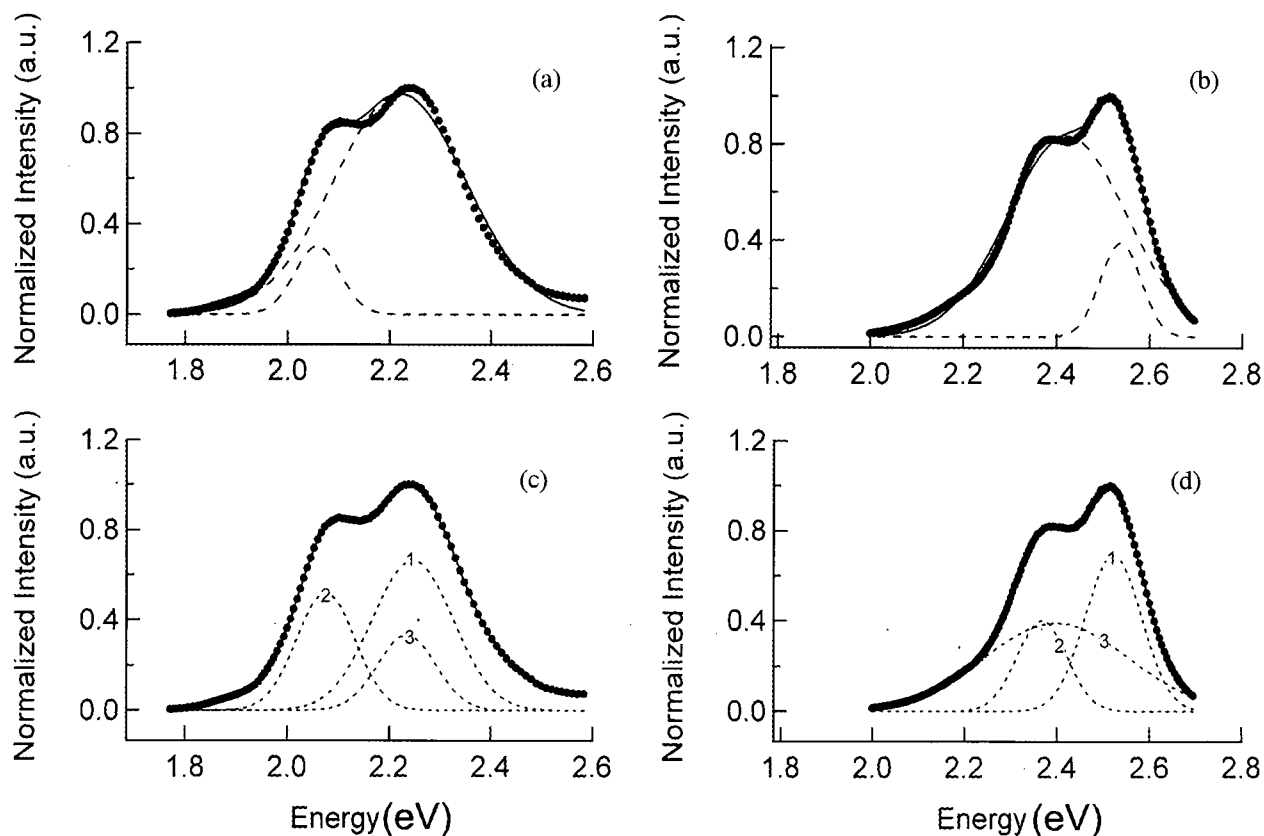


Figure 4.4: Two-Gaussian fits for (a) Anodisc MEH-PPV and (b) Anodisc DP-PPV PL at 77 K and three-Gaussian fits for (c) Anodisc MEH-PPV and (d) Anodisc DP-PPV PL at 77 K. In all cases, the dashed lines show the individual Gaussians, and the solid lines show the sum of the Gaussians.

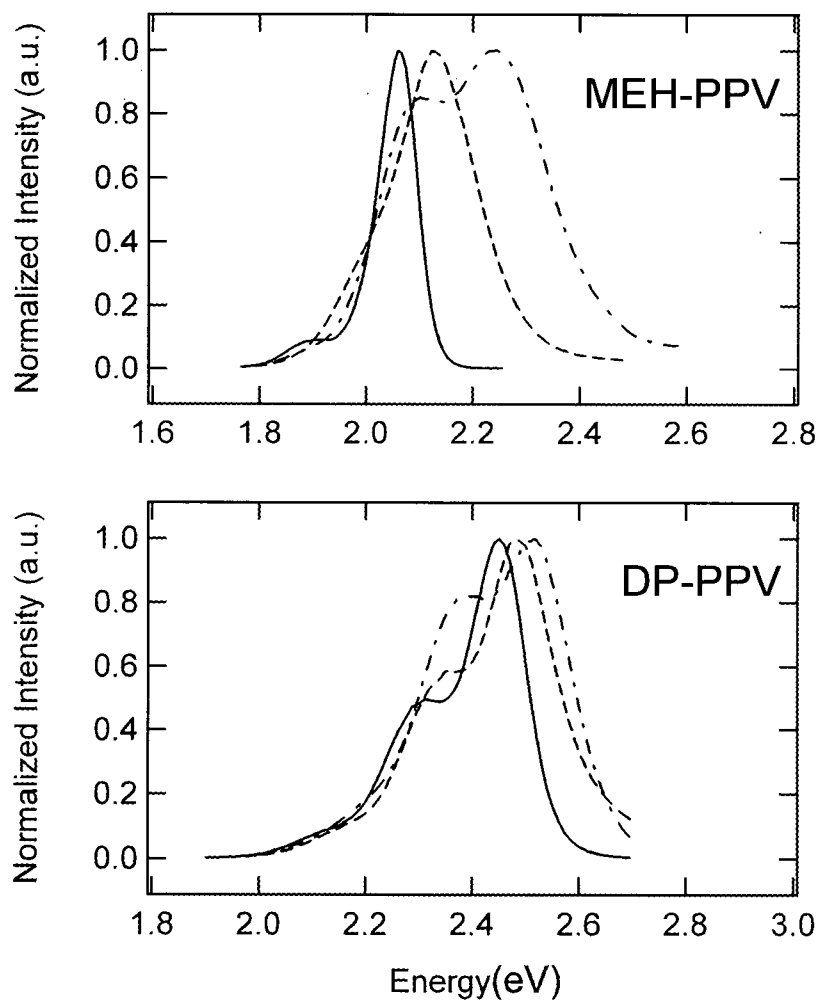


Figure 4.5: Normalized 77 K PL spectra of MEH-PPV and DP-PPV for bulk (solid lines), Anodized (dashed lines) and Anodisc (dash-dotted lines) samples. Excitation wavelength was 398 nm.

4.1.2. Temperature Dependence

The effects of temperature on the time-integrated photoluminescence of bulk MEH-PPV, bulk DP-PPV and anodized DP-PPV are plotted in Figure 4.6. The data shows that both bulk and nanostructured samples exhibit similar temperature dependences. The S_{0-0} and S_{0-1} peaks red-shift with decreasing temperature, which is attributed to the freezing out of torsional modes of the phenylene rings [29], resulting in a longer effective conjugation length and a lower emission energy.

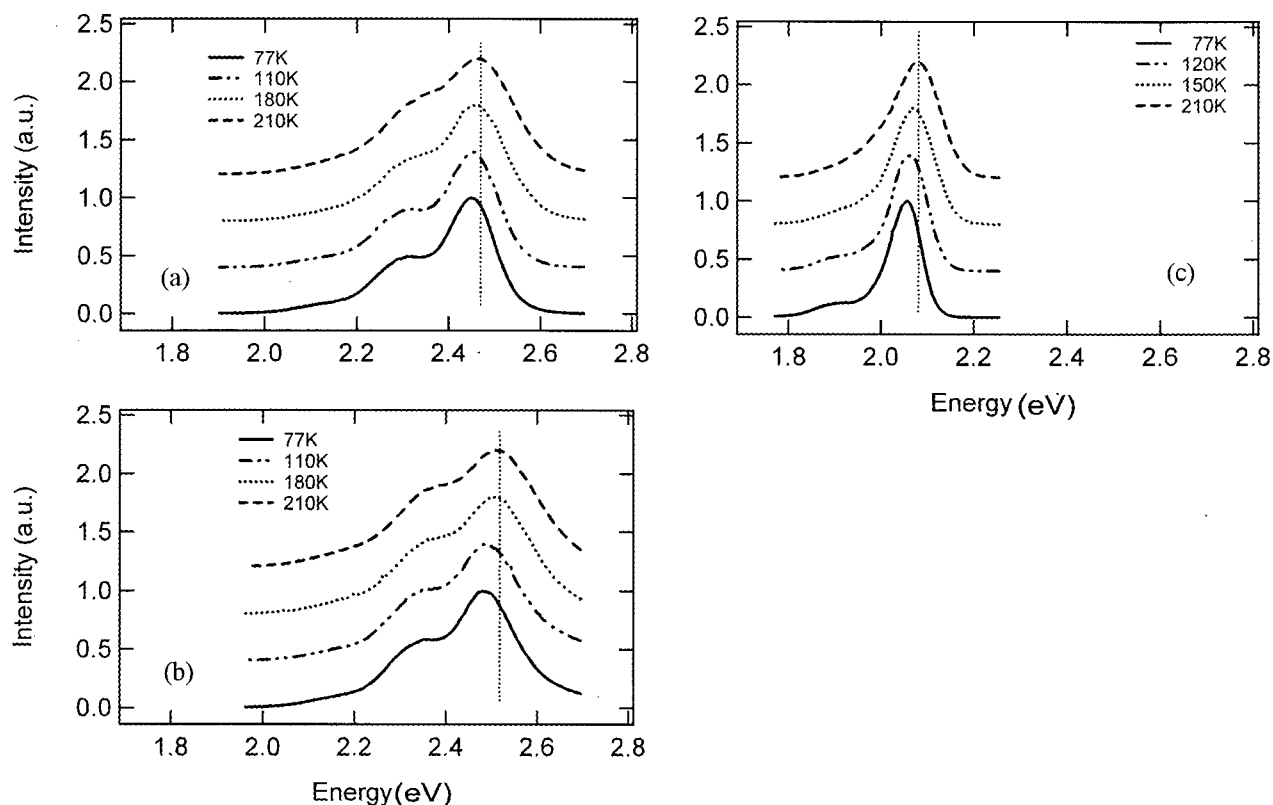


Figure 4.6 : Effects of Temperature on the time-integrated photoluminescence of (a) bulk DP-PPV, (b) anodized DP-PPV and (c) bulk MEH-PPV. Excitation wavelength was 398 nm.

4.1.3 Excitation Intensity Dependence

With an excitation wavelength of 397 nm, the 77 K PL spectra of bulk DP-PPV have been measured at different excitation powers, as shown in Figure 4.7 (a). The intensity of the PL (at 510 nm) as a function of the excitation intensity is plotted in Figure 4.7 (b). The intensity of excitation I_{ex} was monitored by inserting neutral density slides into the excitation beam path. The power of the excitation without any neutral density filter in place was 0.1 mW.

Figure 4.7 (a) shows that the shape of the PL spectrum does not depend on the excitation intensity. In Figure 4.7 (b), I_{pl} is found to be proportional to $I_{ex}^{1.2}$, where the power 1.2 has an error of ± 0.2 . The response of the system is therefore linear within the experimental uncertainty.

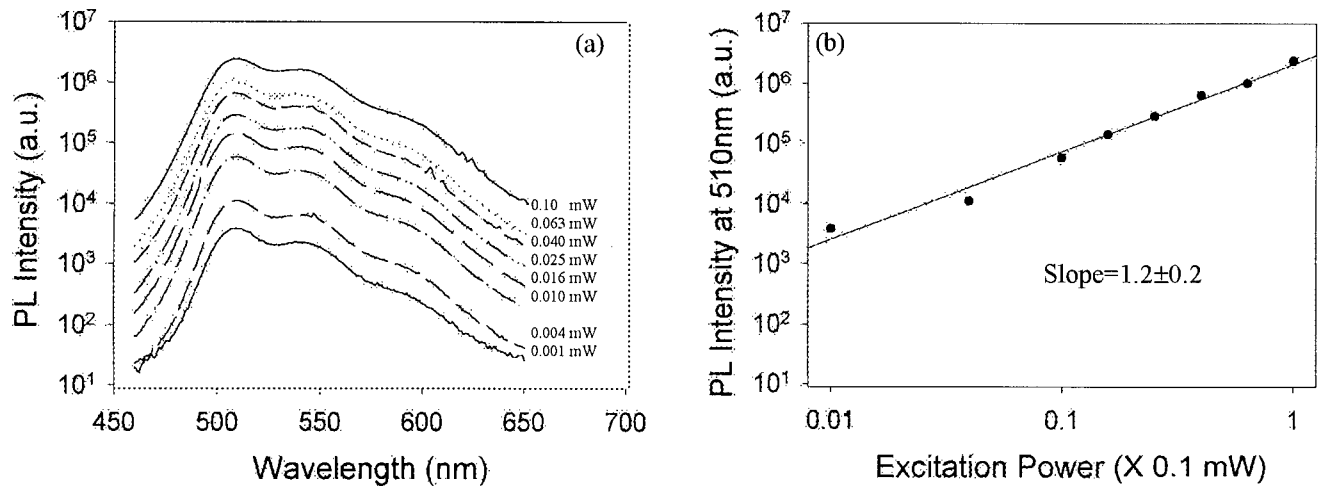


Figure 4.7: Intensity of bulk DP-PPV PL at 77 K versus excitation intensity. Wavelength of excitation was 397 nm.

4.1.4 Comparison of PL intensity from different samples

With the same excitation power of ~ 0.1 mW and same excitation wavelength of 400 nm, the intensity of the PL for different polymers in different forms varies significantly. In Figure 4.8, the PL spectra of bulk and nanostructured MEH-PPV and DP-PPV at 77 K are plotted. Among the six spectra, the PL intensity of bulk MEH-PPV is the strongest, almost ten times stronger than bulk DP-PPV. The PL intensities of the two nanostructured MEH-PPV

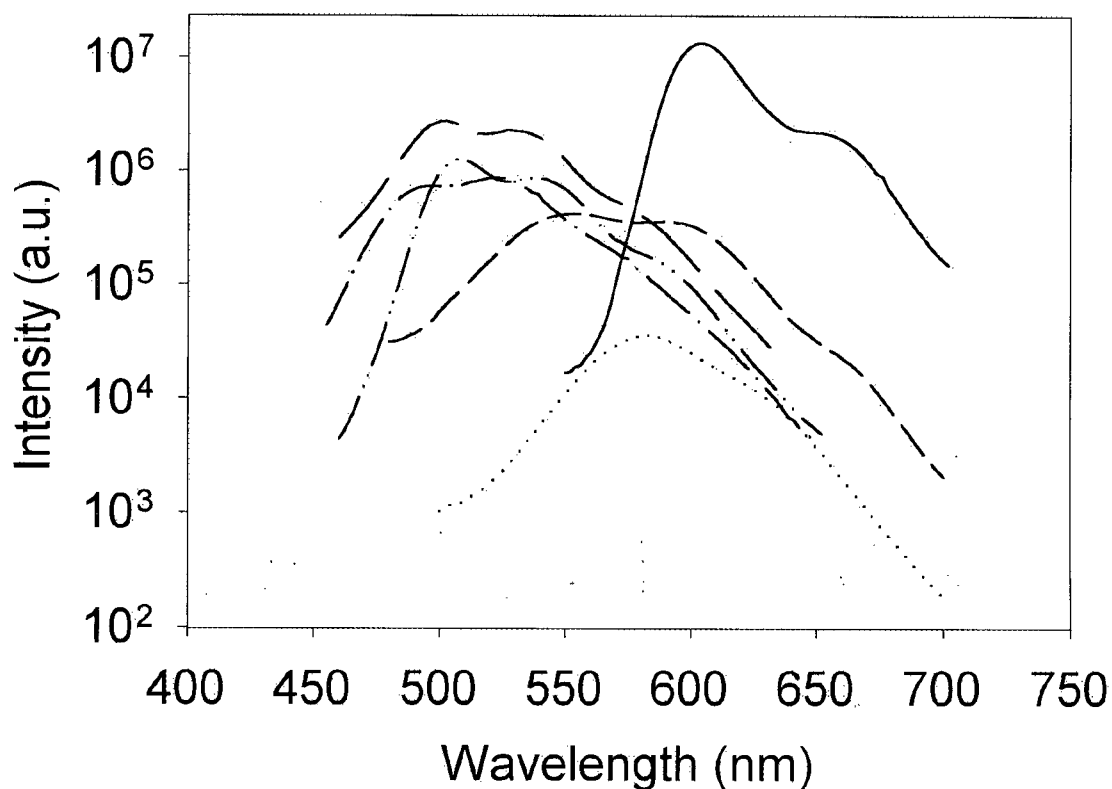


Figure 4.8: 77 K Photoluminescence spectra of MEH-PPV and DP-PPV in bulk and nanostructured forms. Solid line: bulk MEH-PPV, Short dashed line: Anodisc MEH-PPV, Dotted line: Anodized MEH-PPV, Long dashed line: Anodized DP-PPV, Solid line single dot: bulk DP-PPV, Solid line double dots: Anodisc DP-PPV. Excitation wavelength was 400 nm.

samples reduced by factors of 100 and 1000 from the bulk for the anodized and anodisc hosts, respectively. On the other hand, the intensities of the bulk and both nanostructured DP-PPV samples are similar, and considerably stronger than nanostructured MEH-PPV. It is tempting to interpret these results as implying that encapsulation has a strong quenching effect on MEH-PPV, but not on DP-PPV. Unfortunately, there is currently too little knowledge about the relative or absolute polymer incorporation efficiencies in the nanoporous materials to draw any firm conclusions from this data. Its main significance here is to explain why it was impossible to obtain time-resolved data on nanostructured MEH-PPV.

4.1.5 Photodegradation

While both bulk and nanostructured samples exhibit photodegradation, the effect is stronger in the nanostructured samples. Figure 4.9 shows a series of 77 K PL spectra obtained at different delays under constant excitation conditions for Anodisc MEH-PPV and Anodisc DP-PPV. It took about one minute to obtain each spectrum. It is noticed that the shape of the spectra does not change appreciably with photo-degradation. The intensity of the PL at the $S_{0,0}$ peaks of Anodisc MEH-PPV and Anodisc DP-PPV are plotted versus exposure time in Figure 4.10. The intensity of the Anodisc MEH-PPV PL dropped by a factor of 2.3 in 60 minutes after which it continues to decay, but at a slower rate. On the other hand, the intensity of Anodisc DP-PPV PL dropped by a factor of 2 in 20 minutes, after which it remains quite stable.

When the time-resolved experiment was carried out on Anodisc DP-PPV, for each detection wavelength, a fresh spot on the sample was exposed to the excitation beam for 20 minutes. Data in Mode-I was then acquired after the PL intensity stabilized.

In summary, based on the experimental results in Section 4.1.4 and 4.1.5, bulk MEH-PPV is the most intense emitter. Time-resolved experiments were performed on bulk MEH-PPV using the PMT as the sum frequency signal detector. bulk and Anodisc DP-PPV are the less intense emitters, so time-resolved experiments on them were performed using the liquid nitrogen cooled CCD. nanostructured MEH-PPVs are the least intense emitters and their upconverted signals could not be detected even using the CCD.

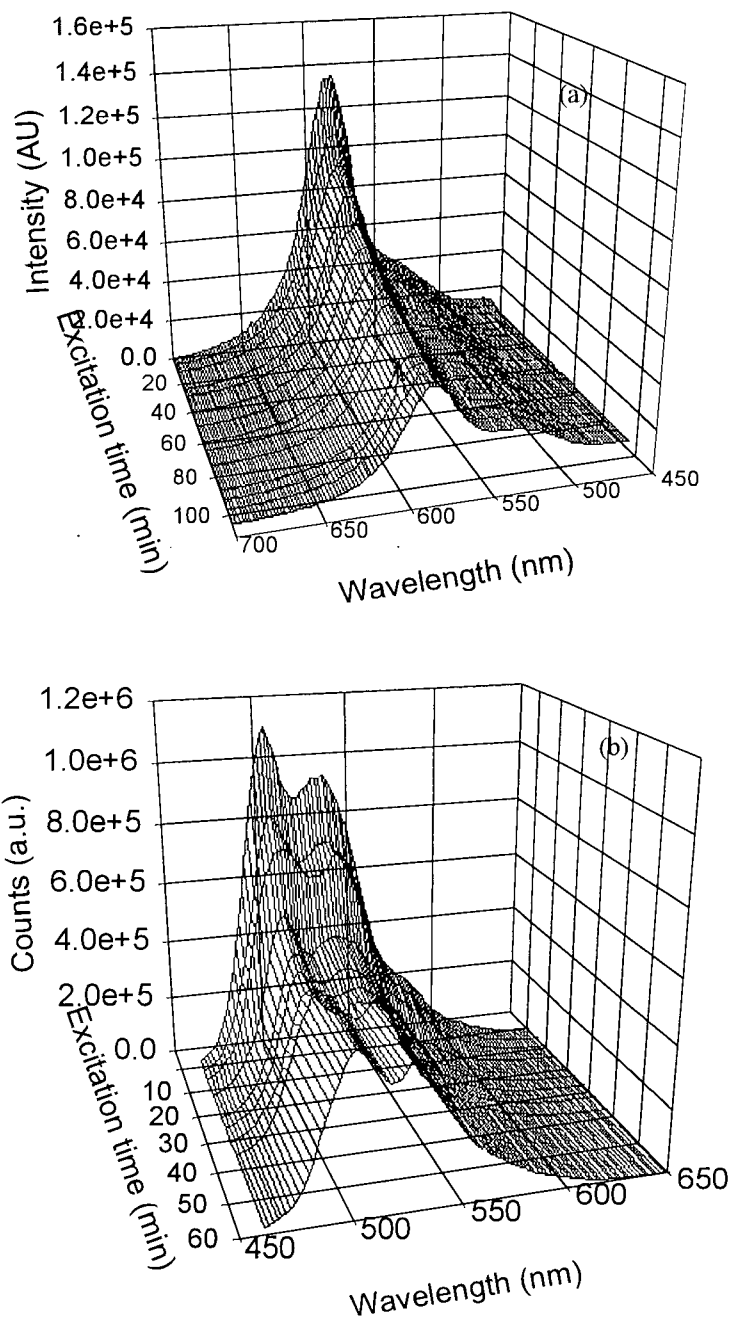


Figure 4.9: Evolution of Spectra of (a) Anodisc MEH-PPV and (b) Anodisc DP-PPV with excitation time. Wavelength of excitation was 400 nm.

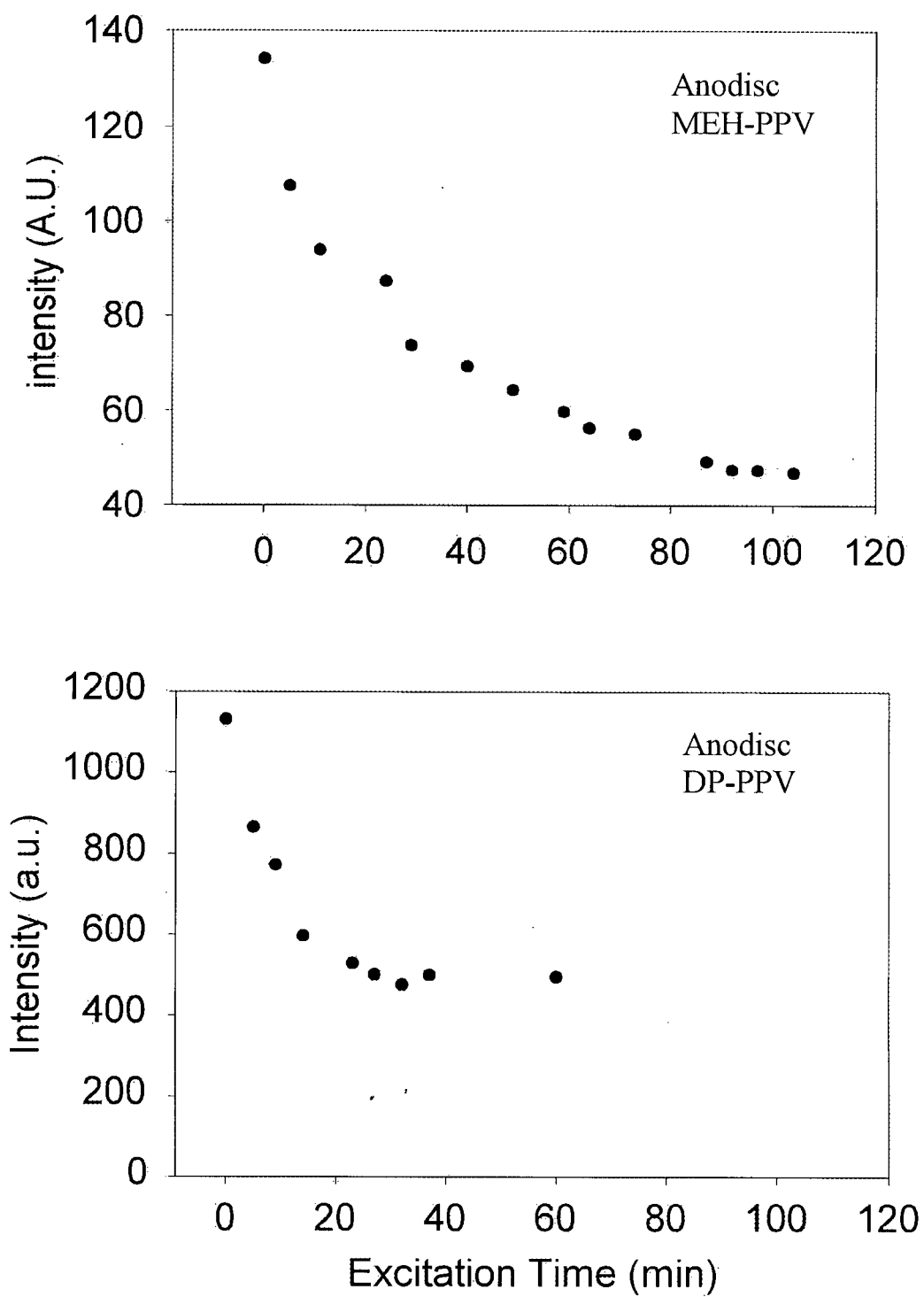


Figure 4.10: Photodegradation of Anodisc MEH-PPV and Anodisc DP-PPV as obtained by the intensity of their respective S_{0-0} peaks.

4.2 Time-resolved Spectra

4.2.1 Phase-matching calibration

As described in section 3.3.6, a tungsten lamp, which is equivalent to a 3200K-blackbody radiation source, was used to evaluate the effectiveness of the Maple code used to estimate the phase-matching angle. The angle between the gate beam and the white light was set to $16.5^\circ \pm 0.1^\circ$, the same angle used in time-resolving experiments performed on bulk MEH-PPV film. The measured upconverted spectra at different crystal orientation angles are plotted in Figure 4.11. Considering the asymmetric nature of the spectra, a function of form

$I = I_0 + A_1 \exp\left(-\frac{(\lambda - \lambda_0)^2}{W_1}\right) + a\lambda$ was used to fit them. Figure 4.12 plots the wavelength (λ_0 in

the equation) at which the upconversion mixing efficiency is the maximum for a given angular position of the nonlinear crystal, as obtained from the fits, compared to the predictions from the Maple code in Appendix A.

The above results show that the Maple code can give a good prediction for the phase matching angle with a small offset. The actual wavelengths of peak conversion efficiency are all $\sim 0.2^\circ$ greater than that predicted by the Maple Code for a given gate/PL geometry. In Figure 4.12, the error bars originate from the accuracy of the gate/PL angle ($\pm 0.1^\circ$) and the curve fitting to the white-light upconversion spectra have been taken into consideration.

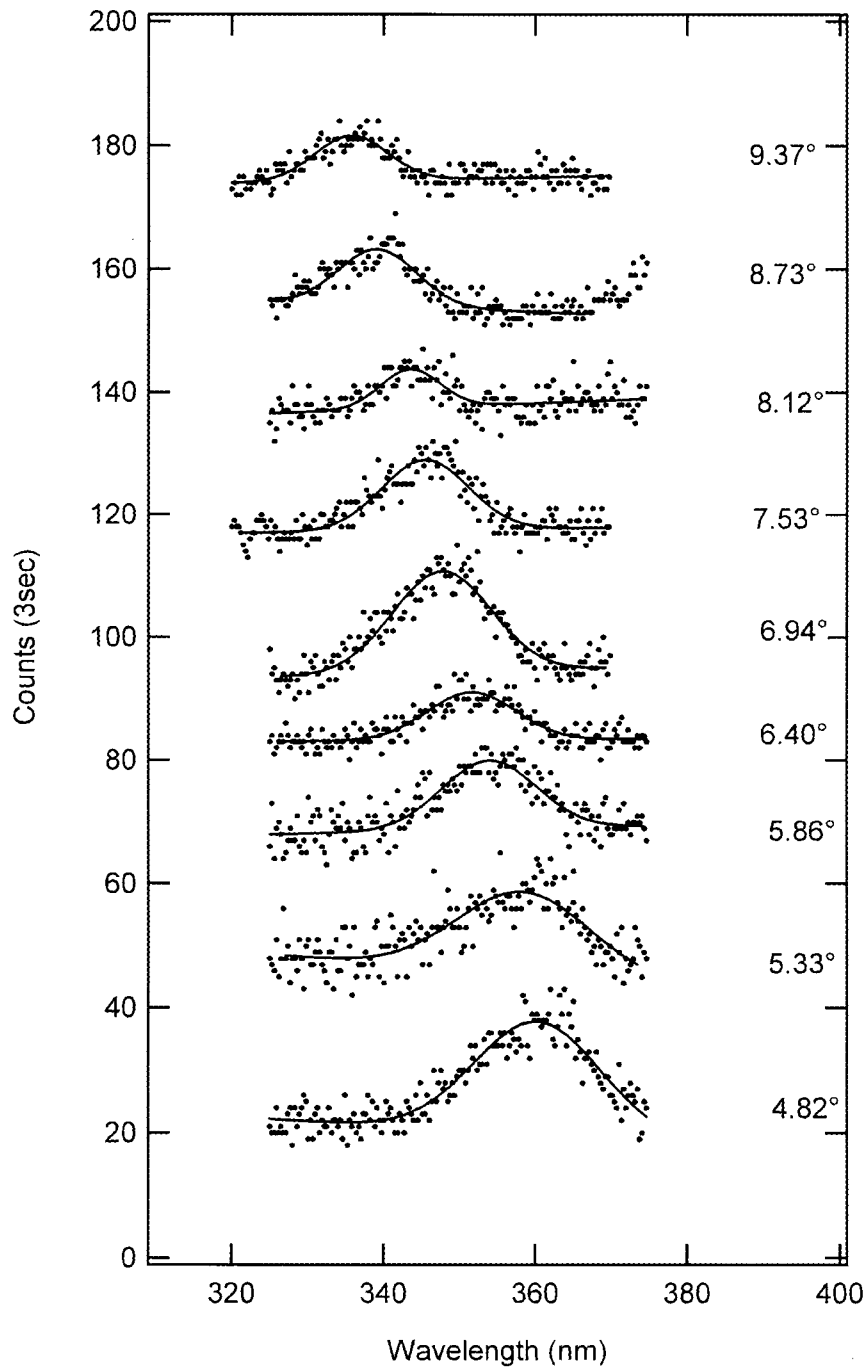


Figure 4.11 : White light upconversion spectra at different crystal orientation angles (incident angle of the gate, θ_{2i} in Figure 2.4). Solid line is the fit obtained as described in section 4.2.1. Wavelength of the gate: 797.5 nm.

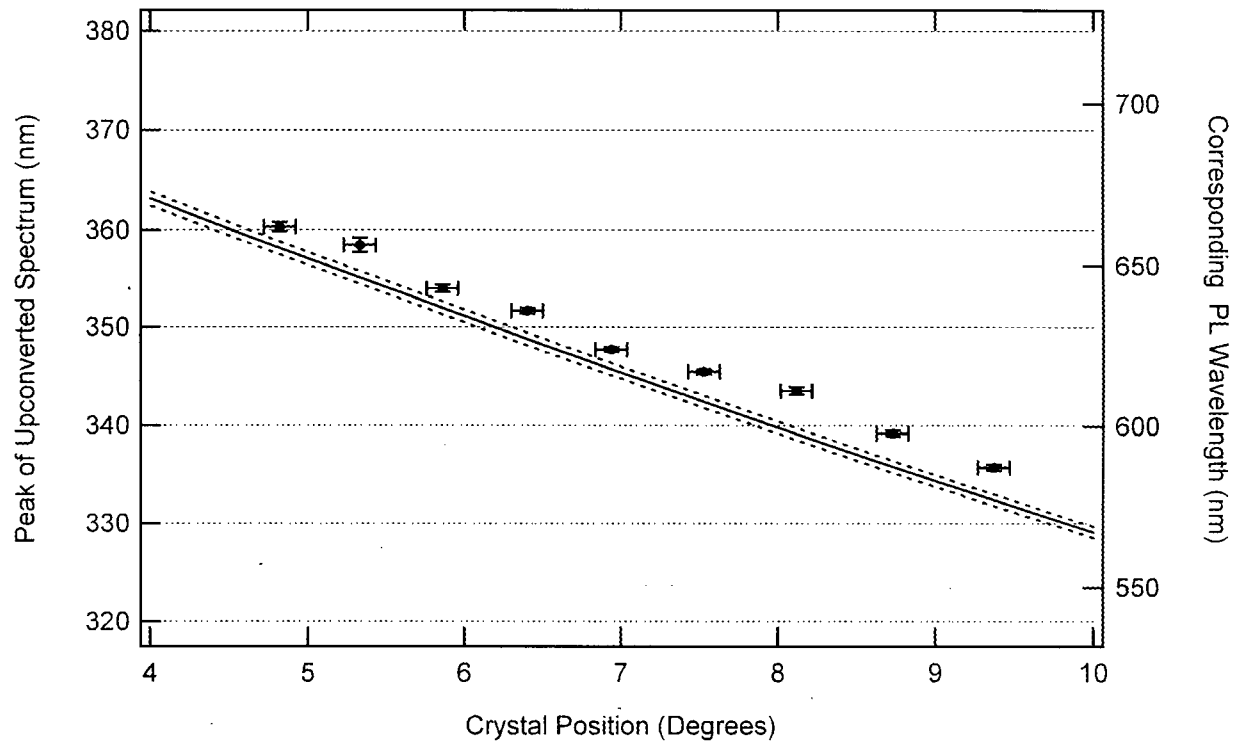


Figure 4.12: Solid dot: Wavelength at which the mixing efficiency is maximum for a given angular position of the nonlinear crystal, obtained from Figure 4.7. Solid line: results predicted by the Maple code in Appendix A (angle between the gate and the PL beams is 16.5°). Dotted lines: results predicted by the Maple code when the angles between the gate and PL beams are 16.4° and 16.6° .

4.2.2 Bulk MEH-PPV

The photoluminescence of bulk MEH-PPV at 77 K was time-resolved using the upconversion technique described in Chapter 3. We first consider the decay profiles that are measured using data collection Mode I. The decay at short time delays (0-20 ps) is plotted in Figure 4.13. The full decay curves (0-500 ps) are plotted in Figure 4.14. From these plots one can see two distinct regimes in the data: a fast decay which occurs on timescales less than 20 ps, followed by a slower tail which extends to hundreds of picoseconds. Following the approach of McCutcheon's on bulk PPV decay profiles [18], the data that decrease monotonically with delay were fit to a bi-exponential function of the form

$$I = I_0 + w_1 e^{-t/\tau_1} + w_2 e^{-t/\tau_2}, \quad (4.1)$$

where I_0 is a constant background, τ_1 and τ_2 represent the short and long time constants, respectively, and w_1 and w_2 are the respective weighting factors. The fits are superimposed on the data points in Figure 4.14, and match the experimental data well.

In Figure 4.15(b), the extracted fast and slow time constants are plotted versus the corresponding detection energies. These time constant data points can be categorized into three groups; each group is represented by a circle. Based on the model described in Reference [18], the time constants in the 0-0 group are associated with the pure electronic transition $S_{0,0}$, while the time constants in the 0-1 group are associated with one-phonon assisted transition $S_{1,0}$, and the time constants in the 0-2 group are associated with two-phonon assisted transition $S_{2,0}$.

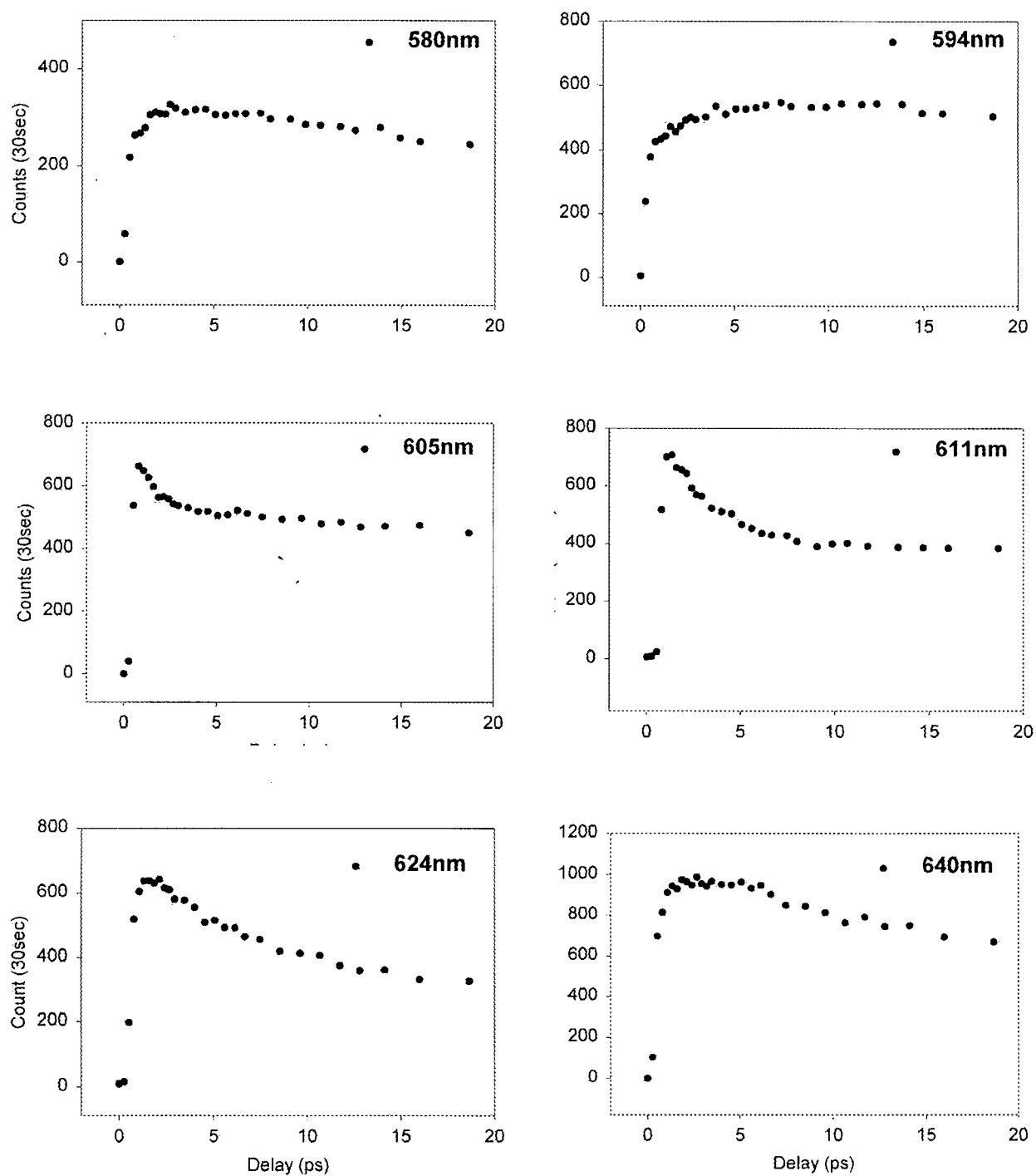


Figure 4.13: Short time regime of time-resolved bulk MEH-PPV photoluminescence at 77 K.

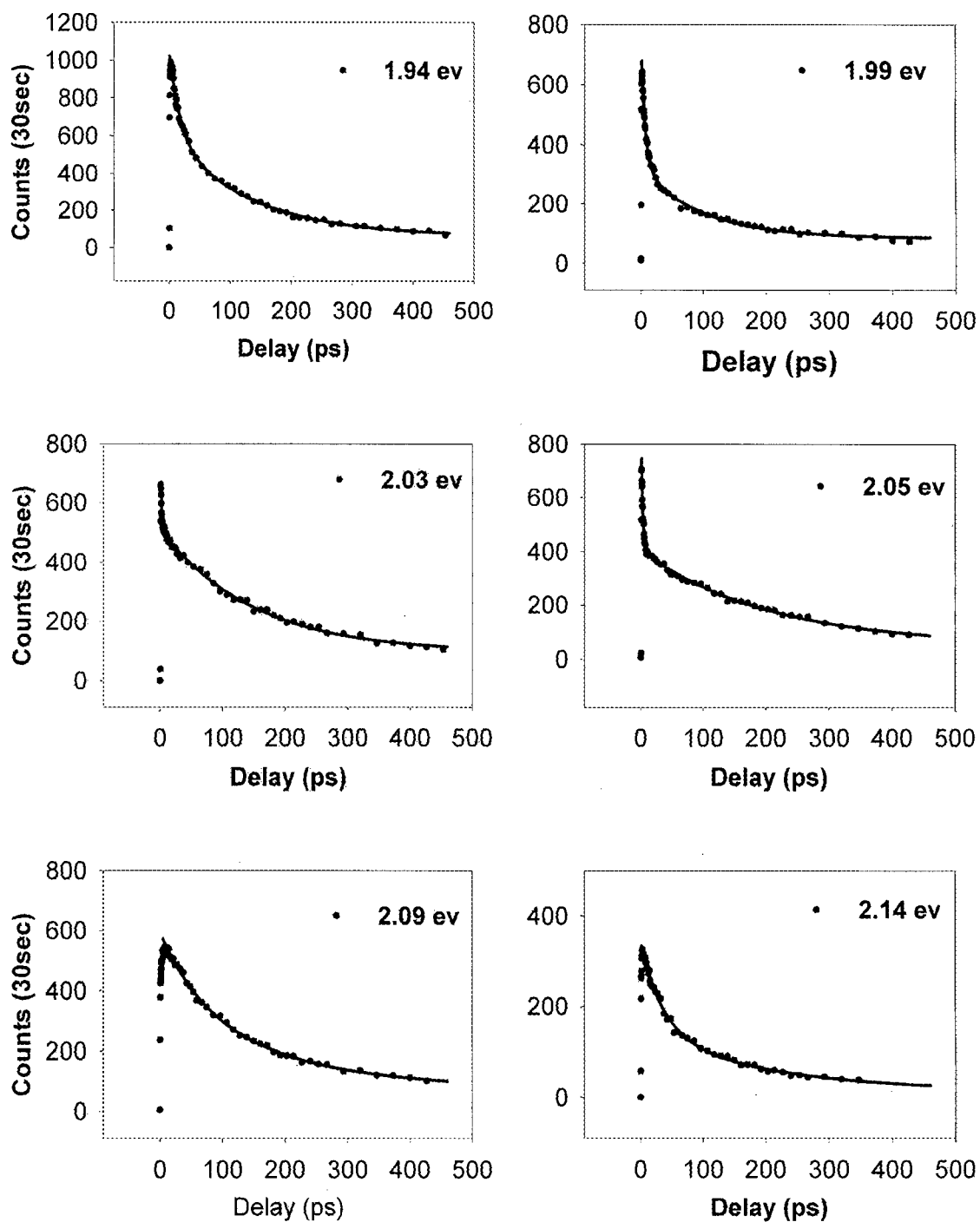


Figure 4.14: Bi-exponential fits of time-resolved bulk MEH-PPV photoluminescence at 77 K.

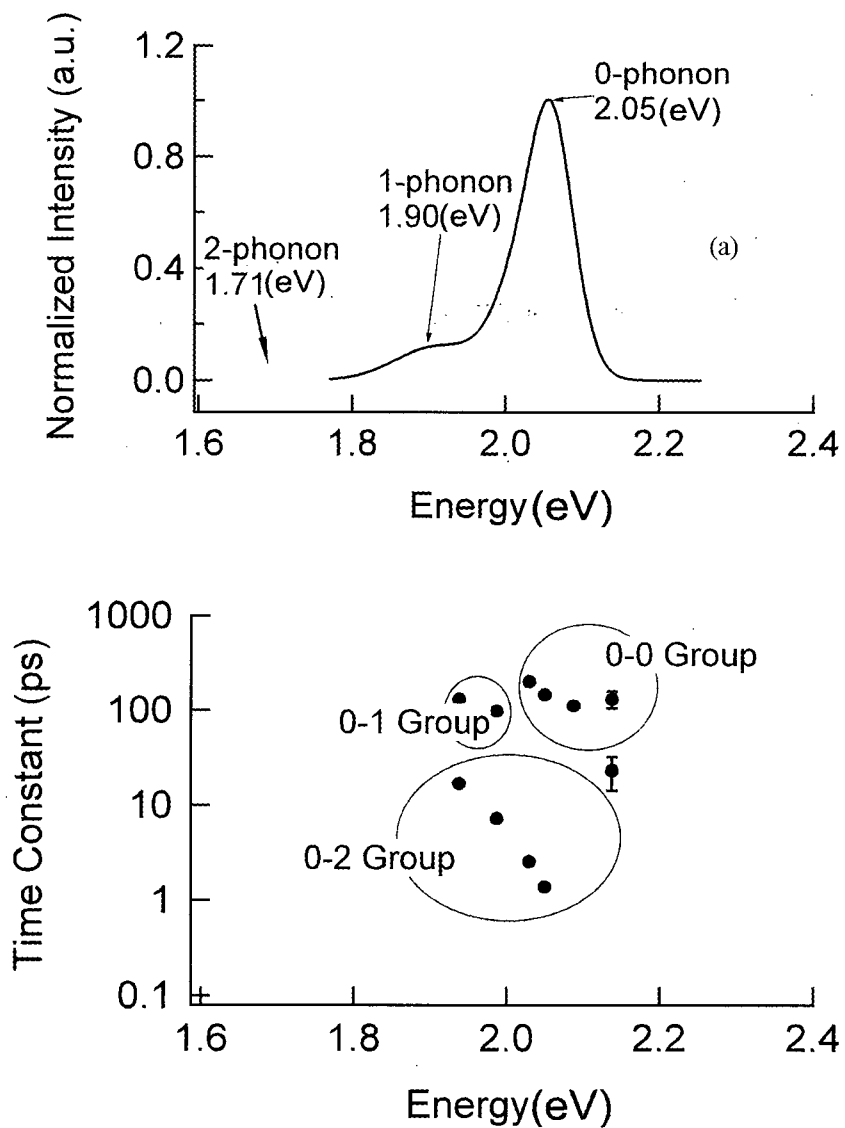


Figure 4.15: Time constants extracted from the time-resolved decay profiles using the Bi-exponential fits.

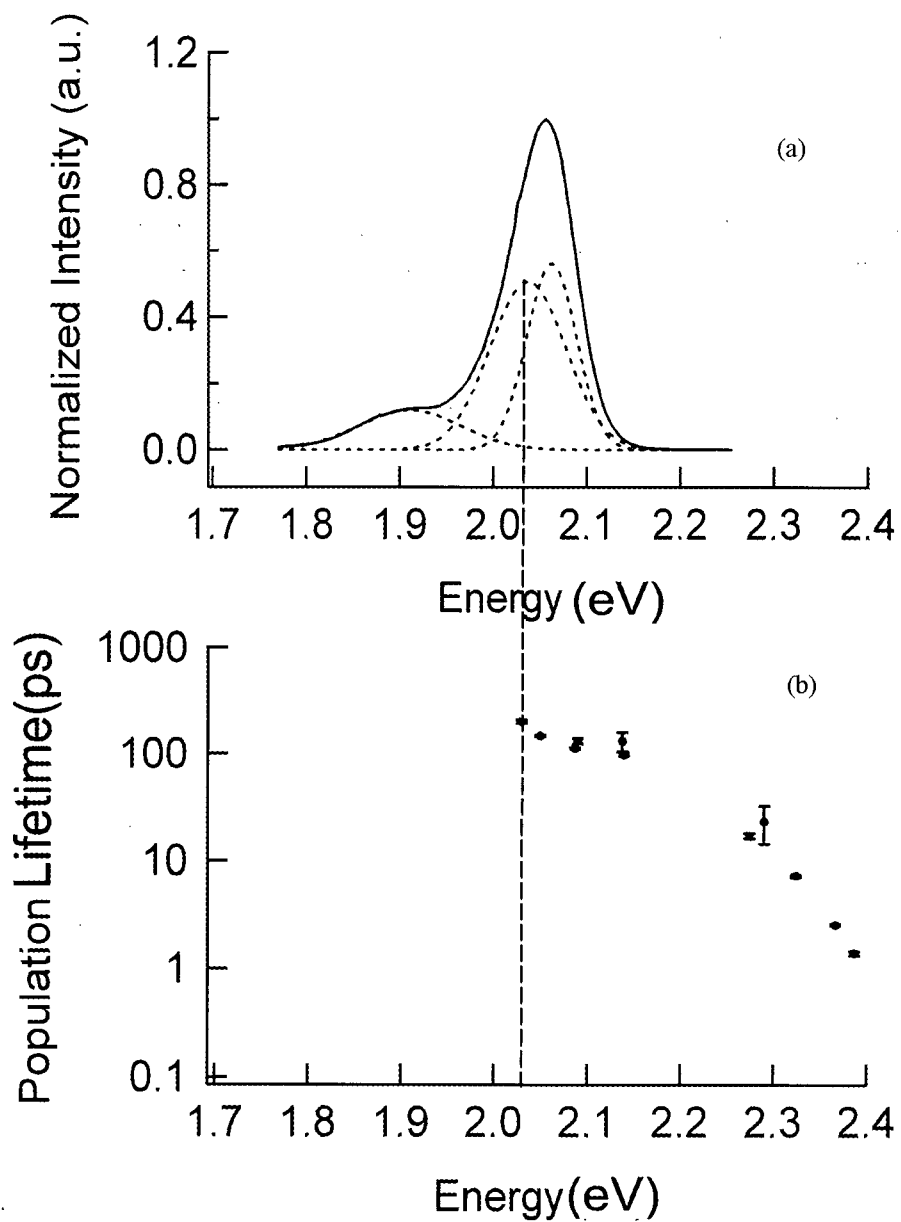


Figure 4.16 : Population lifetime versus estimated electronic energy. Time-integrated spectrum in (a) includes the 3-Gaussians used to obtain an excellent fit to the data. (see Section 4.1).

We consider the time constants to be associated with a single DOS of the ECL of the coherent segments of the polymer chains, but that DOS is manifest via 0-0, 0-1 and 0-2 transitions. Thus to obtain a consistent energy dependence for the time constants, the points in 0-1 and 0-2 groups are translated one phonon energy 0.153 eV and two phonon energies 0.337 eV to higher energy, respectively. The one phonon energy was determined by measuring the energy separation between first and second Gaussians in the 3-Gaussian fit discussed in Section 4.1.1. As the 2-phonon transition peak is not in the range of our measurement, the two phonon energy of 0.337 eV was derived from the photoluminescence spectra in Reference [37].

In Figure 4.16, the translated time constants are plotted versus the estimated energy of the associated coherent segments. For energies above the 0-0 peak in the time-integrated spectrum (actually above the intermediate energy Gaussian shown in Figure 4.15(a)), the population lifetime decreases with increasing energy. This behavior is very similar to that obtained on PPV, the parent conjugation polymer of MEH-PPV, by McCutcheon [18], as shown in Figure 4.17. The explanation of our results reinforces the hypothesis raised in Reference [18].

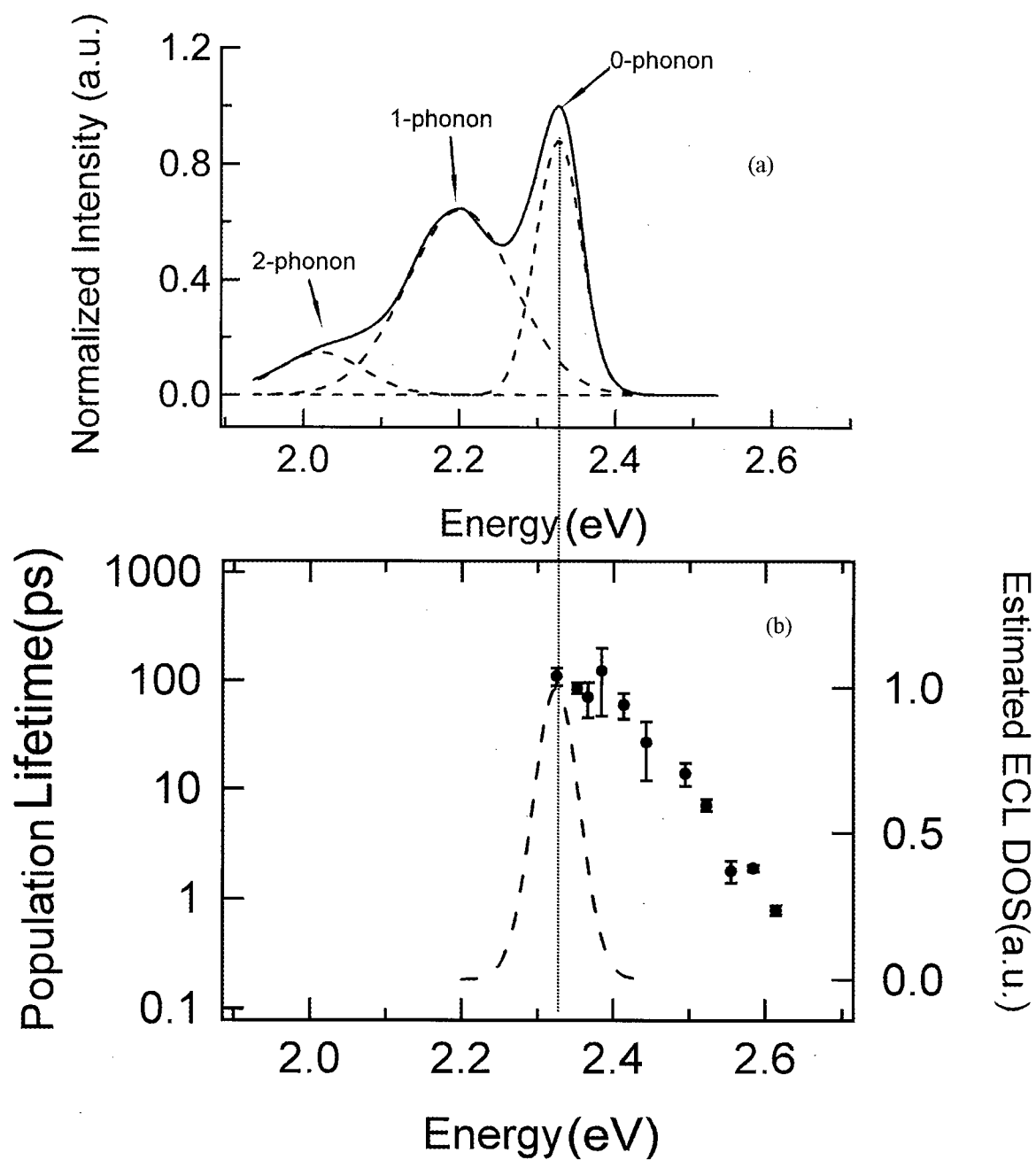


Figure 4.17: Population lifetime versus ECL energy for bulk PPV, the parent polymer of MEH-PPV, at 77 K, from Reference [18]. (a) Bulk PPV PL at 77 K with three Gaussian fit in dashed line. (b) The dashed line is the estimated ECL density of states (DOS) from the 0-0 transition peak of the bulk PPV PL at 77 K.

4.2.3 Bulk DP-PPV

Time-resolved experiments on bulk DP-PPV at 77 K were performed with probing energies at 2.23 eV, 2.27 eV, 2.30 eV, 2.36 eV, 2.43 eV and 2.50 eV, as shown in Figure 4.18. The intensity of the PL from bulk DP-PPV is less than one tenth that of bulk MEH-PPV. The peak intensity of the upconverted signal is ~ 3 counts per second, which was almost the same as the dark counts from the PMT. A LN/CCD detector was therefore used in place of the PMT as the photo detector (see Section 3.3.7). As in Section 4.2.2, a bi-exponential function was used to fit the decay profiles, and the results are plotted in Figure 4.18, along with the data.

Within the latitude allowed by the signal to noise ratio, the bi-exponential fits reproduce the data points reasonably well. However, for the 495 nm (2.50 eV) profile, a tri-exponential function was used to give a better fit, resulting in a 20% reduction of the chi-squared value. As the error of the longest time constant is very large (1500 ± 13500 ps), the longest life constant is omitted. In Figure 4.19 the extracted time constants are plotted versus probe energy. Again, the time constants can be categorized into three groups. After translating them by the one-phonon energy (0.15 eV) for the 0-1 group and the two-phonon energy (0.34 eV) for the 0-2 group, respectively, we obtain the time constants as a function of coherent segment energy, as shown in Figure 4.20. The one-phonon energy (0.15 eV) was obtained by measuring the separation of the first and second Gaussians of the three-Gaussian fits to the time-integrated PL spectrum of bulk DP-PPV, as discussed in Section 4.1.1. The 2-phonon peak is actually a small “bump”. The position of the “bump” is at 2.11 eV, the two-phonon energy is therefore

estimated to be 0.34 eV, very close to the results quoted in Reference [36]. The symmetric inhomogeneously broadened ECL density of states obtained from the three-Gaussian fit in Section 4.1.1 is also plotted. Again, the population lifetime decreases with the increasing energy, or the decreasing ECL of the coherent segments in the polymer.

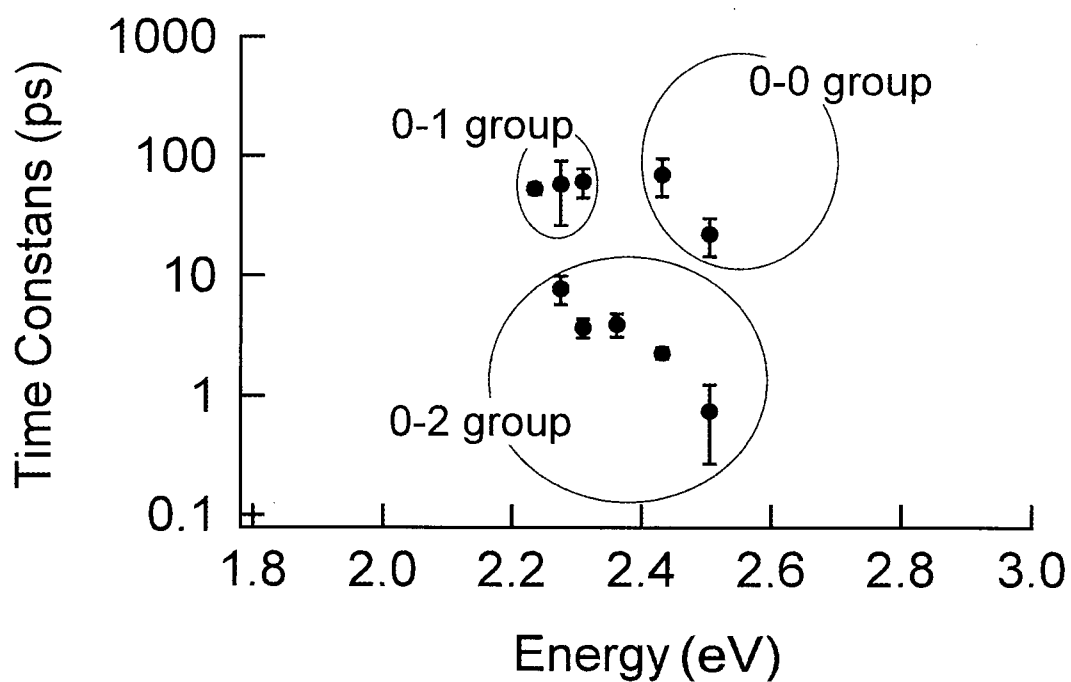


Figure 4.19 : Extracted time constants versus probe energy for bulk DP-PPV PL at 77 K.

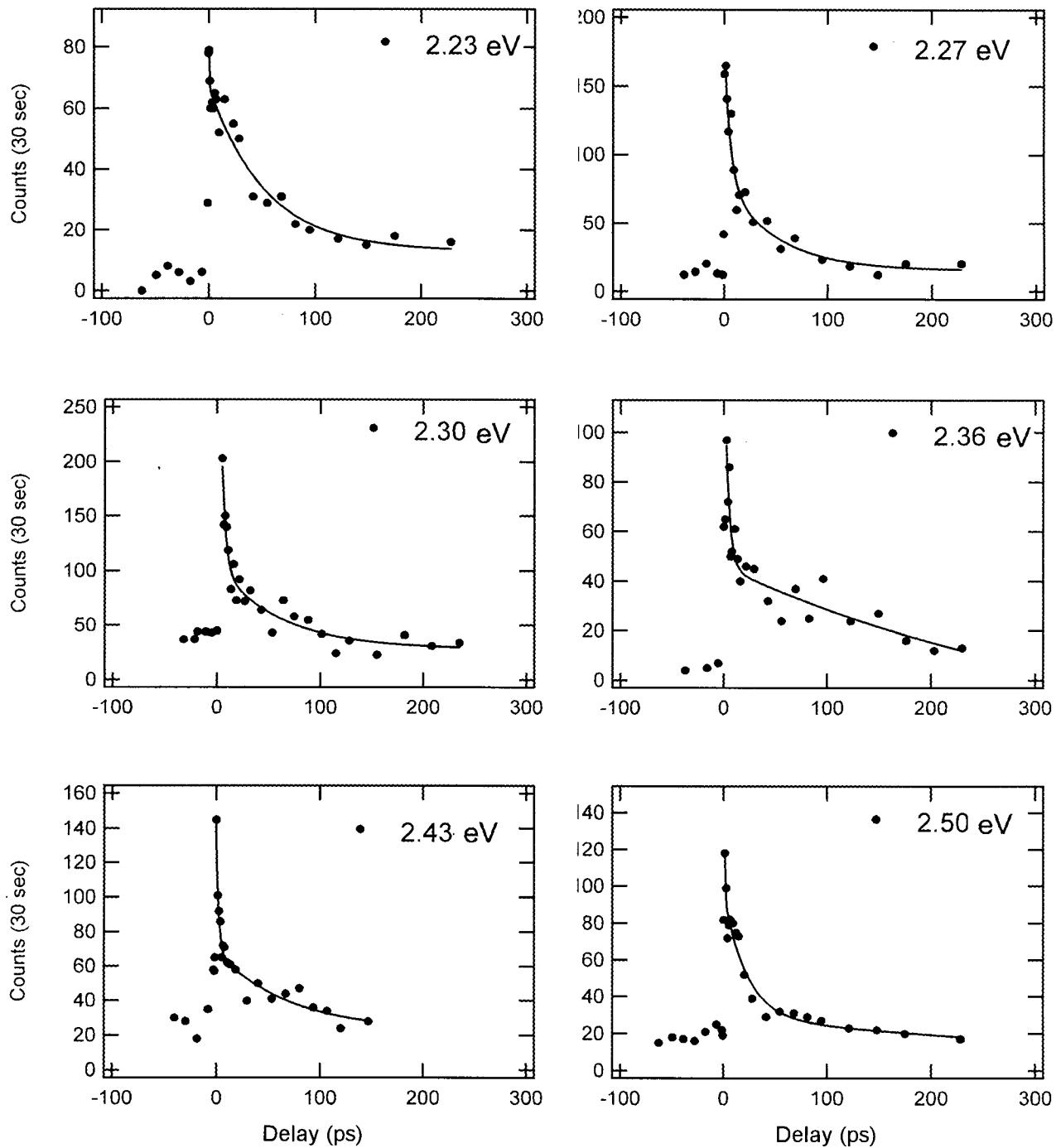


Figure 4.18: Time-resolved profiles for bulk DP-PPV photoluminescence at 77 K.

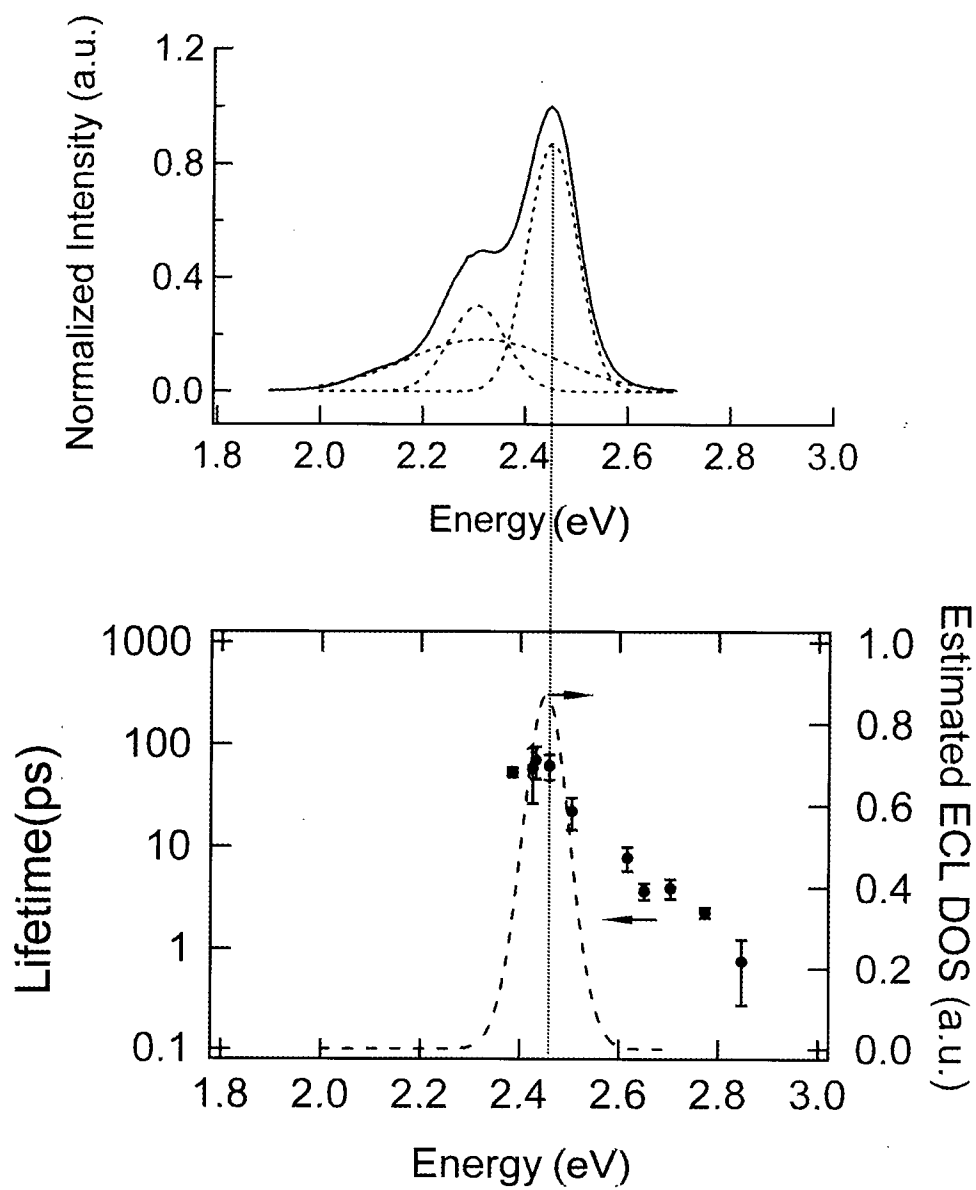


Figure 4.20: Population Lifetime versus estimated energy of the corresponding coherent segments for bulk DP-PPV at 77 K.

4.2.4 Anodisc DP-PPV

Time-resolved experiments were performed on Anodisc DP-PPV at 77 K at probe energies of 2.30 eV, 2.36 eV, 2.43 eV, 2.54 eV and 2.58 eV. At 77 K the intensity of the Anodisc DP-PPV PL is similar to that of the bulk DP-PPV. The LN/CCD detector was therefore used to detect the upconverted signal. The bi-exponential function was again used to fit the decay profiles, and the results are shown with the data in Figure 4.21. Similar to bulk DP-PPV and bulk MEH-PPV, the bi-exponential fits reproduce the data points reasonably well. However, here for the 480 nm (2.58 eV) profile, a tri-exponential function was used to give a better fit resulting in a 20% reduction of the chi-squared value. But as the longest lifetime has a very large error (940 ± 6000 ps), it is omitted. For the 540 nm (2.30 eV) profile, a single exponential was used. In Figure 4.22, the extracted time constants are plotted versus probe energy. Again, the time constants are categorized into three groups and translated by the one-phonon energy (0.15 eV) for the 0-1 group and the two-phonon energy (0.34 eV) for the 0-2 group, respectively. Again, the one-phonon energy (0.15 eV) was obtained by measuring the separation of the first and second Gaussians of the three-Gaussian fits to the time-integrated PL spectrum of Anodisc DP-PPV, as per discussed in Section 4.1.1. As expected the one-phonon energy is the same as that obtained from bulk DP-PPV. The 2-phonon transition peak in Anodisc DP-PPV time-integrated PL spectrum is not obvious. As the encapsulation of polymer chains into the nanopores should not change the structures of the material, it is assumed that both the bulk and Anodisc DP-PPV have the same energy separation between the first and second vibrational levels in the S_0 state. Thus the two-phonon energy was taken to be the same as that obtained from bulk DP-PPV.

The results after shifting are shown in Figure 4.23. Again, the symmetric inhomogeneously broadened ECL density of states obtained from the three-Gaussian fit in Section 4.1.1 is also plotted, and the population lifetime decreases with the increasing energy, or the decreasing ECL of the coherent segments in the polymer. It is noticed that the dependence on the ECL energy below the DOS peak becomes more flat as compared to that above the DOS peak.

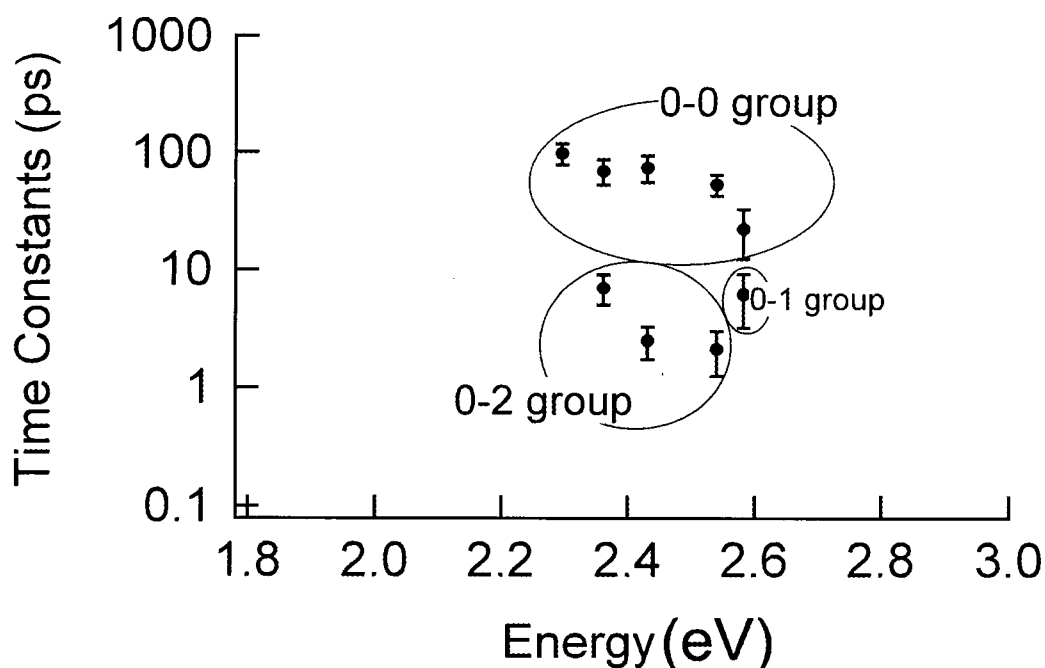


Figure 4.22: Extracted time constants versus probe energy for Anodisc DP-PPV PL at 77 K.

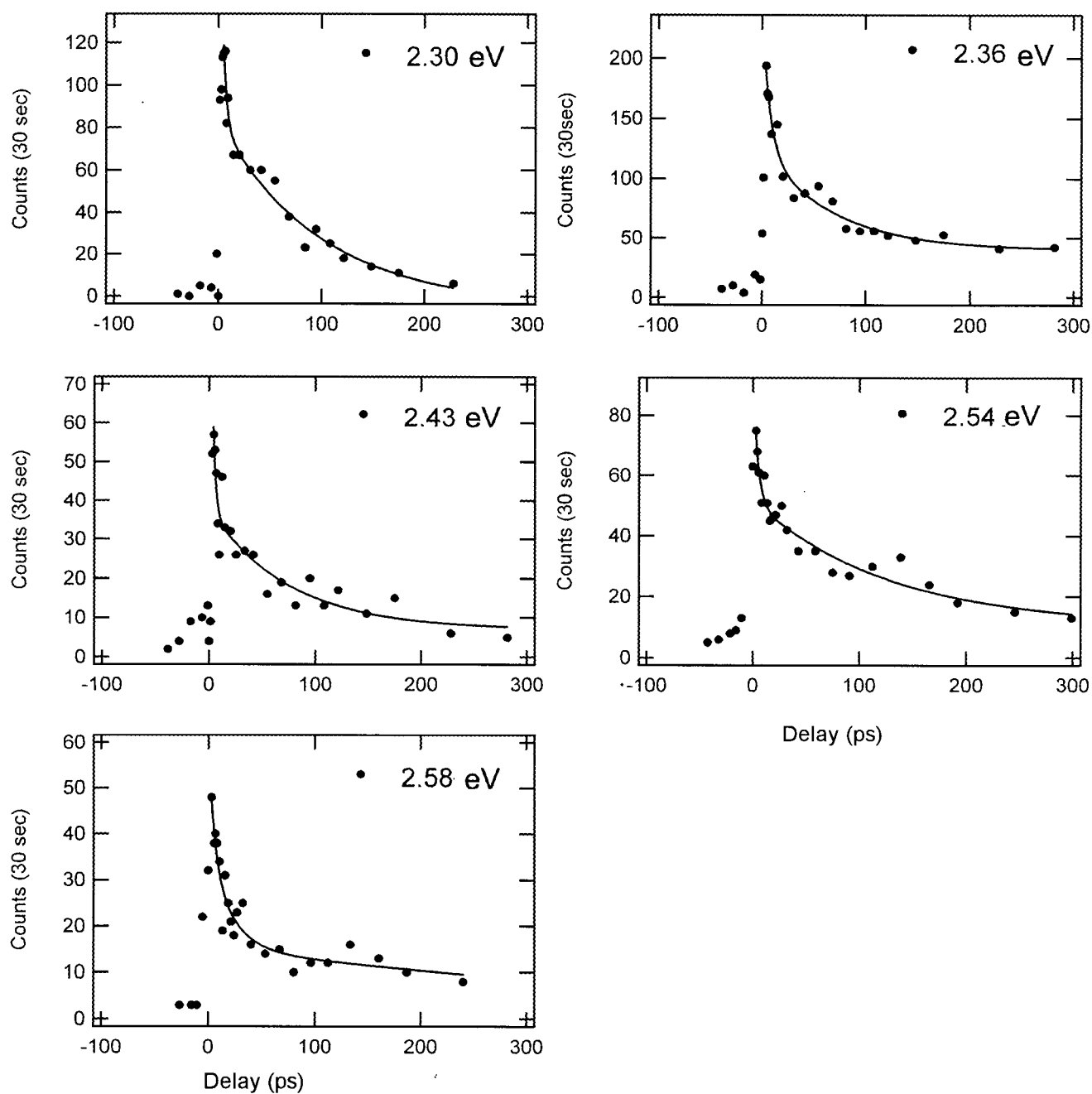


Figure 4.21 : Decay profiles for Anodisc DP-PPV photoluminescence at 77 K.

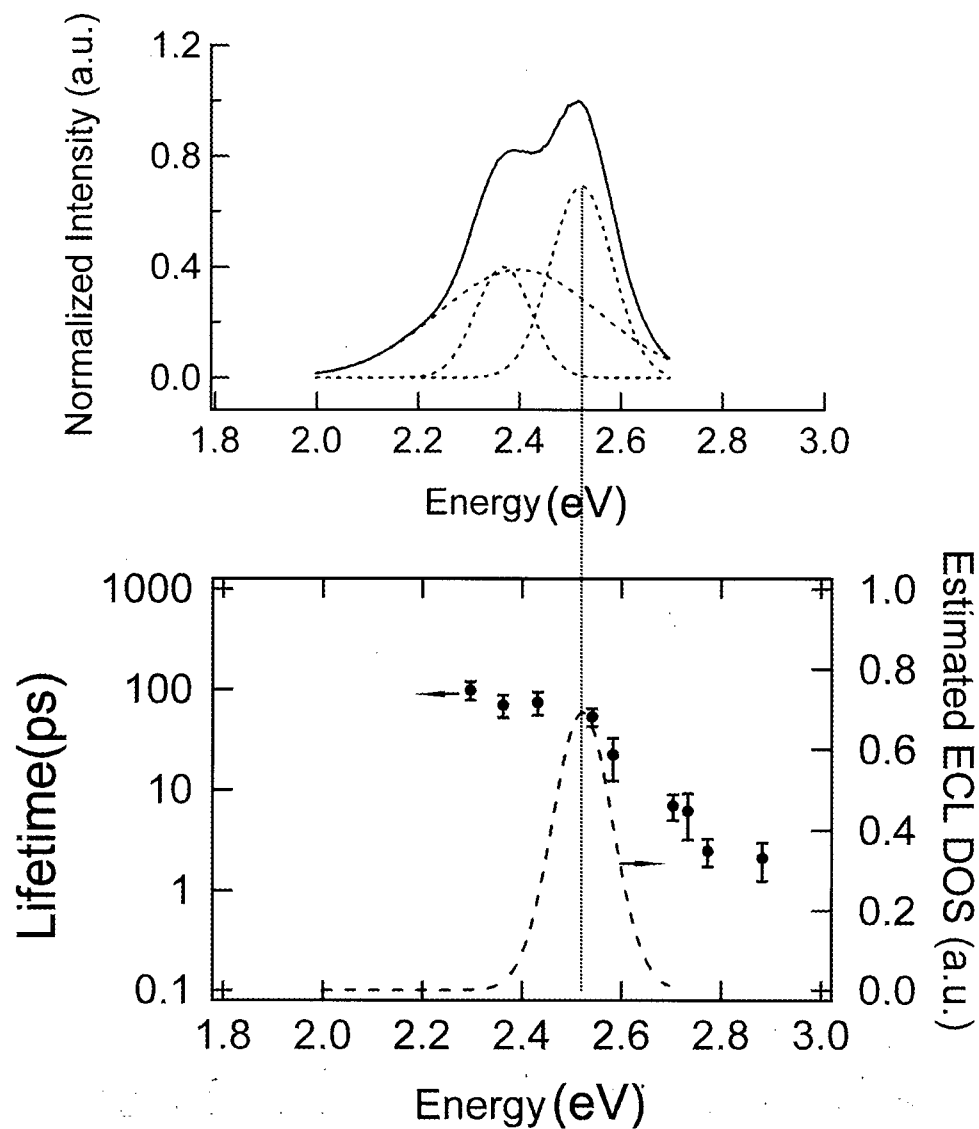


Figure 4.23 : Population lifetime versus estimated energy of the corresponding coherent segment for Anodisc DP-PPV.

4.2.5 Bulk vs. Anodisc DP-PPV: Lifetime Dependence on Energy

The population lifetime dependence on energy for both bulk DP-PPV and Anodisc DP-PPV shown in Figure 4.20 and Figure 4.23 look similar. Figure 4.24 shows both sets of data on the same graph for easy comparison. The time constants for Anodisc DP-PPV have been shifted -0.068 eV, the blue-shift energy extracted from the time-integrated spectra of bulk and Anodisc DP-PPV as discussed in section 4.1.1, so that the peaks of DOSs associated with the 0-0 peaks are aligned. The dependence of population lifetime on the estimated ECL energy for the coherent segments, near and above the respective ECL energy DOS peaks, are *remarkably* similar for the bulk and Anodisc DP-PPV.

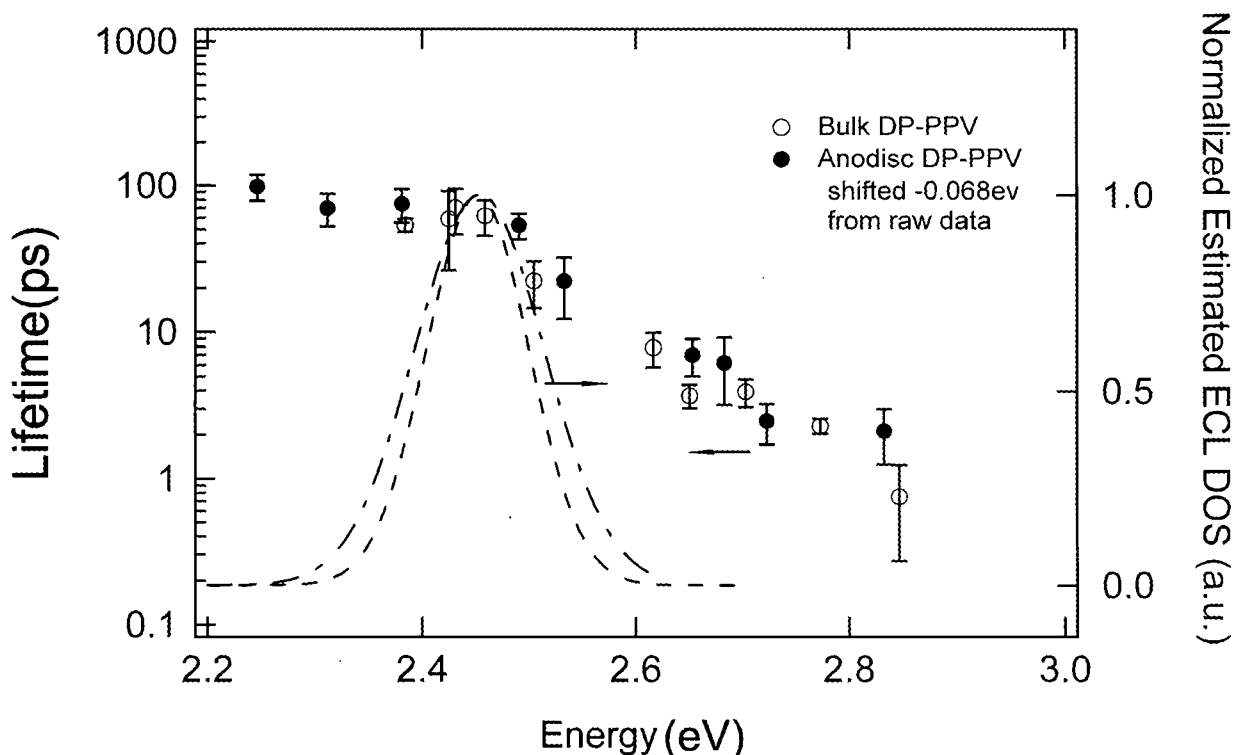


Figure 4.24: Comparison of population lifetimes of bulk and Anodisc DP-PPV. Time constants of Anodisc DP-PPV have been shifted -0.068 eV, the blue-shift energy of the 0-0 transition extracted from the time-integrated spectra of bulk and Anodisc DP-PPV, to align the DOS peaks, shown in dashed line for bulk DP-PPV and dot-dashed line for Anodisc DP-PPV.

4.2.6 Bulk MEH-PPV vs. Bulk PPV: Lifetime Dependence on Energy

The population lifetime dependence on energy for both bulk MEH-PPV and bulk PPV shown in Figure 4.16 and Figure 4.17 also look similar. To compare them, Figure 4.25 shows their population lifetime constants on the same graph for easy comparison. The time constants of bulk MEH-PPV have been shifted $+0.289$ eV, the energy difference of the respective 0-0 transition peaks, so that the estimated ECL DOS peaks are aligned. The population lifetimes of bulk MEH-PPV are significant longer than those of bulk PPV, but their dependence on the energy with respect to the peak in the respective DOS is very similar.

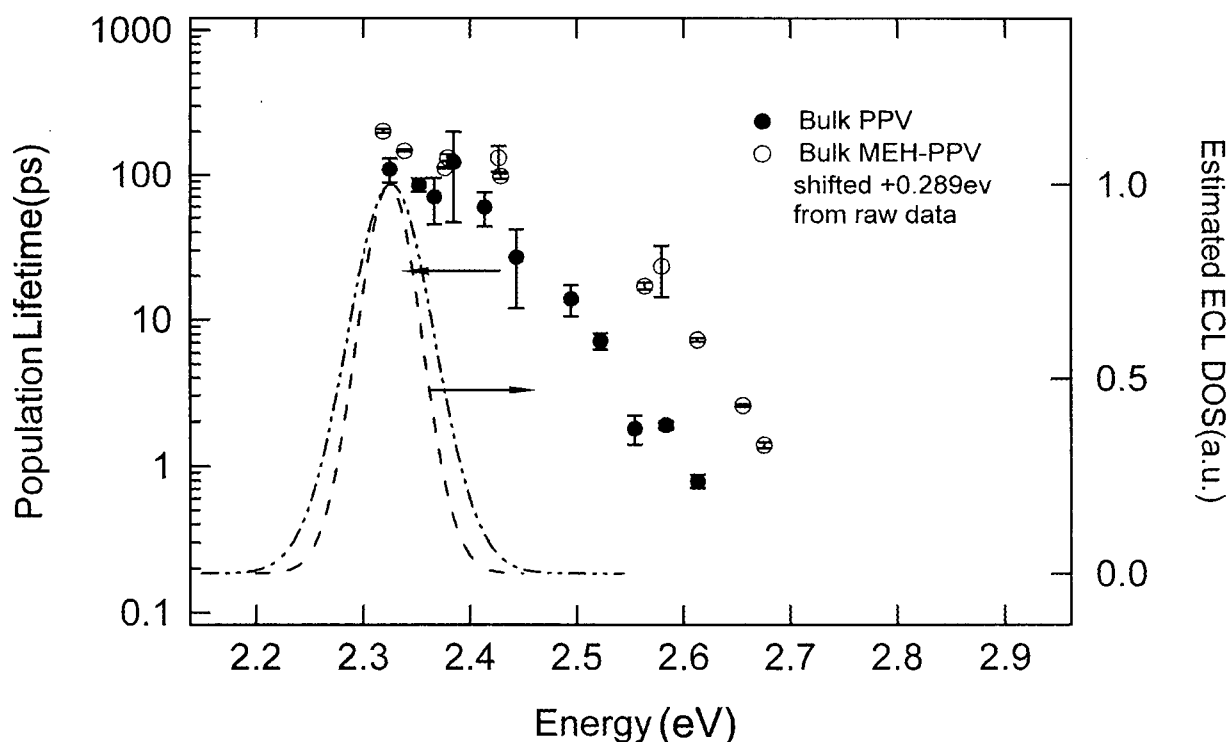


Figure 4.25: Comparison of population lifetimes of bulk PPV and bulk MEH-PPV. Time constants of bulk MEH-PPV have been shifted $+0.289$ eV, the energy difference of the 0-0 transition extracted from the time-integrated spectra of bulk PPV and bulk MEH-PPV, to align the DOS peaks, shown in dashed line for bulk PPV and dot-dot-dashed line for bulk MEH-PPV.

4.2.7 Lifetime dependence on Energy for PPV and derivatives

In Figure 4.26, the population lifetime constants of bulk PPV, bulk MEH-PPV, bulk DP-PPV and Anodisc DP-PPV are shown on the same graph with the respective 0-0 transition peaks aligned for easy comparison. For clarity, all the error bars are omitted. The energy dependences of the lifetimes in PPV and these two PPV derivatives in bulk and different encapsulated forms are quite similar.

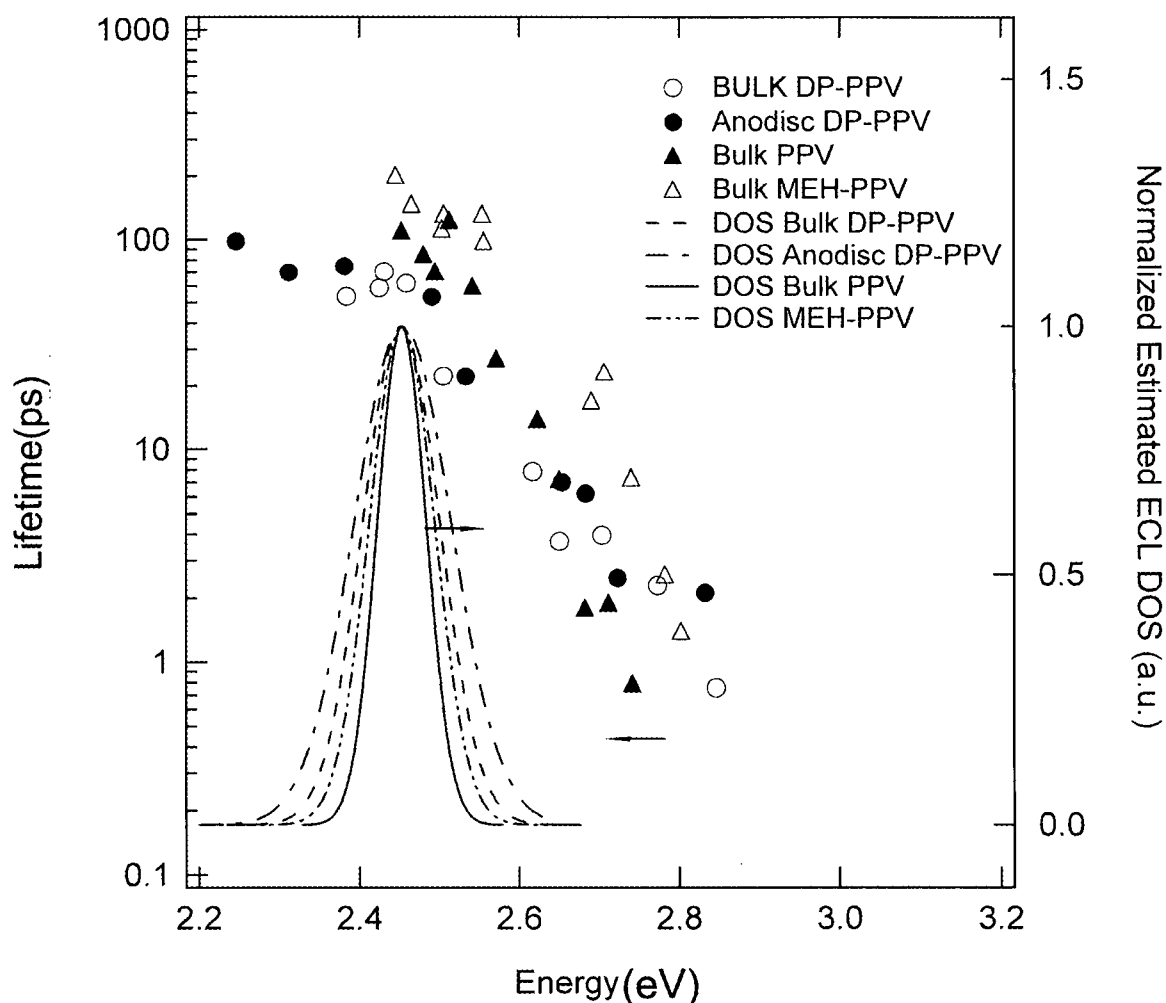


Figure 4.26: Comparison of population lifetimes of PPV and its derivatives MEH-PPV and DP-PPV, in bulk or in Anodisc forms. Time constants of bulk PPV, bulk MEH-PPV and Anodisc DP-PPV have been shifted $+0.128$ eV, $+0.416$ eV and -0.068 eV, respectively, to align their respective 0-0 transition peaks.

Chapter 5

Summary and Conclusions

5.1 Summary

5.1.1 Experimental Apparatus

A pre-existing photoluminescence upconversion system [18] used to time-resolve the optical emission from bulk PPV polymers was enhanced to increase the achievable signal to noise ratio by a factor of more than three. Using a liquid nitrogen cooled CCD detector, a new nonlinear upconversion crystal, and new alignment procedures, upconverted signals less than ~ 0.3 counts per second have been detected. The tuning curve for the new nonlinear upconversion crystal (BBO cut at 38°) was calibrated by recording the upconverted spectrum obtained using a white-light source at various crystal angles. These enhancements made it possible to time-resolve the emission from MEH-PPV and DP-PPV light emitting polymers, even when they are encapsulated in pores formed in two different types of electrochemically etched alumina.

5.1.2 Effects of Encapsulation on the Time-Integrated Luminescence

Spectrum of MEH-PPV and DP-PPV at 77 K

Members of Dr. M.O. Wolf's group in the Chemistry Department of UBC successfully encapsulated two types of light emitting polymers (MEH-PPV and DP-PPV) in nanoporous alumina. Porous alumina structures made at UBC had pore sizes of 50-90 nm, while porous alumina obtained commercially predominantly consisted of pores with diameters on the order of 200 nm.

The time-integrated photoluminescence spectra of both types of polymers, in bulk form and when they are encapsulated in the two different alumina hosts, were obtained under identical excitation conditions at 77 K. For both polymers, there is a significant blue shift of the 0-0 transition peaks in both nanostructured samples as compared to the bulk samples. Referring to Table 4.2, for the same guest polymer, the Anodisc 13 alumina membrane from Whatman Inc. results in a larger blue shift than the "home-made" anodized alumina. The relative intensity of the 0-1 transition peak (with respect to the 0-0 transition peak) is increased for both nanostructured samples as compared to bulk samples. The relative intensity of the 0-1 transition increases from 25% (bulk) to 81% (Anodisc) for MEH-PPV and from 35% (bulk) to 58% (Anodisc) for DP-PPV. In addition, the spectra of the nanostructured samples are broader than their bulk counterparts. The FWHMs of the 0-0 peaks of Anodisc MEH-PPV and Anodisc DP-PPV PL increased by 100% and 35%, as compared to those of bulk MEH-PPV and bulk DP-PPV, respectively. A relatively strong Gaussian shaped feature distinct from the usual 0-n electronic/vibrational transitions is found to help in quantitatively

fitting the data from the nanostructured samples. There is some evidence of a weaker contribution from this additional feature in the bulk MEH-PPV and DP-PPV spectra.

By comparing the intensities of time-integrated PL for different polymers in different forms, it is tempting to imply that encapsulation has a strong quenching effect on MEH-PPV, but not on DP-PPV. Unfortunately, there is currently too little knowledge about the relative or absolute polymer incorporation efficiencies in the nanoporous materials to draw any conclusions from this data.

5.1.3 Effects of Encapsulation on the Time-Resolved Luminescence Spectrum of MEH-PPV and DP-PPV at 77 K

Time-resolved upconversion experiments were performed on bulk MEH-PPV, bulk DP-PPV and Anodisc DP-PPV. It was found that the population lifetime increases as the ECL of the coherent segments increases above the average segment length, for both bulk and nanostructured polymer samples. When the energy dependence of the population lifetime data for both bulk DP-PPV and Anodisc DP-PPV are shifted in energy by the difference in the respective 0-0 transitions, they exhibit very similar behavior. Applying the same shift to the population lifetime dependence on segment energy for bulk PPV and bulk MEH-PPV, it is found that the shape of the curves are almost identical, but the lifetimes of MEH-PPV are two to three times longer than those of the pure PPV. The similarity of the energy dependence of the lifetimes in pure PPV and these two PPV derivatives in bulk and different encapsulated forms is quite striking.

5.2 Conclusions

The time-integrated photoluminescence spectra from both MEH-PPV and DP-PPV polymers are substantially altered from their bulk form when they are encapsulated in nanoporous alumina. The changes, including blue shifts, broadening, and enhancements in phonon assisted transitions, are all greater for both PPV derivatives when encapsulated in commercial Anodisc material with randomly distributed pores, ~ 200 nm in diameter, as compared to alumina films with 50-90 nm diameter pores arranged in a regular hexagonal array. As the pores in both alumina hosts are considerably larger than the diameter of the polymer molecules, the changes are most likely due to interactions between the polymers and the inside walls of the alumina pores. These results are very encouraging, and suggest that there is significant potential for modifying the optical emission properties of PPV-based polymers by controlling their interaction with alumina surfaces. The significance of the distinct new feature in the time-integrated data from the nanostructured samples is not understood, but it is a relatively large effect that should be pursued.

It is unlikely that this new feature plays a significant role in the emission at short times (less than a few hundred picoseconds), as the energy dependence of the time-resolved data is remarkably similar for all bulk and nanostructured samples when considered with respect to the peak in the respective DOS. All four samples studied with the upconversion system exhibit lifetimes that decrease monotonically, and nearly exponentially with excess energy above the peak in the DOS. This is qualitatively consistent with the interpretation of Kersting et al. [38,39] who attribute the decay dynamics in terms of an intrachain diffusion mechanism of the

photoexcited electron-hole pairs. These results suggest that the interactions with the alumina pore walls does not affect these intrachain dynamics on sub-nanosecond timescales.

These results motivate future studies that should include sample characterization using complementary interface sensitive techniques. The substantial blue shifts observed here in the nanoporous materials, up to 0.183 eV, may prove useful in light emitting device applications if methods are developed to improve the emission efficiency and to reduce photodegradation. Further optical experiments, including analysis of polarization dependences and the influence of magnetic fields at temperatures from 4 K to room temperature are also warranted.

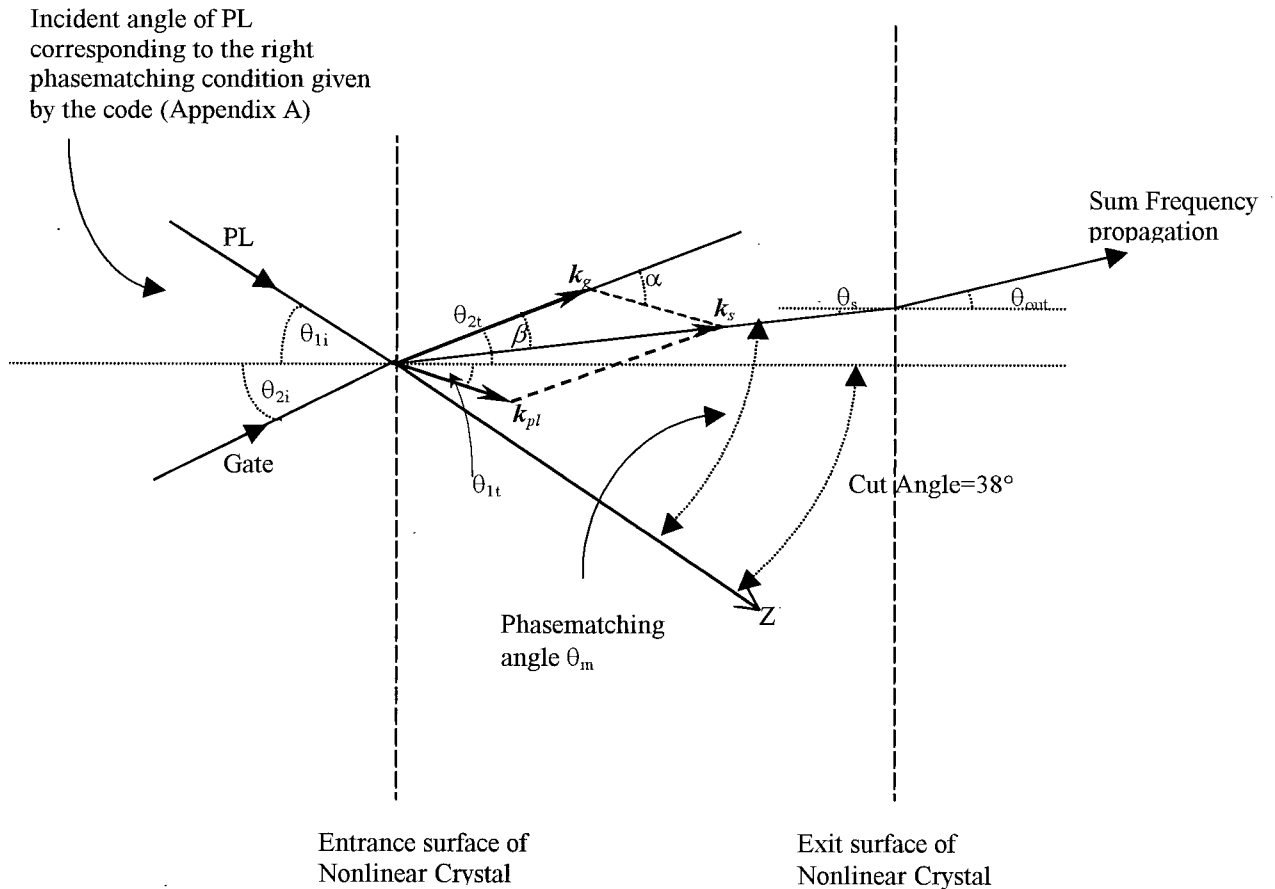
Reference

- [1] D. Braun, *et al.* Appl. Phys. Lett., 58(1991) 1982
- [2] Q. Pei, *et al.* Science, 269(1995) 1086
- [3] G. Yu, *et al.* Science, 270 (1995) 1789
- [4] G. Yu, *et al.* Synthetic Metals, 111-112 (2000) 133
- [5] F. Hide, *et al.* Science, 273 (1996) 1833
- [6] T. Gabler, *et al.* Opt. Comm., 137(1997) 31
- [7] G. Yu, *et al.* Appl. Phys. Lett., 64(1994) 3422
- [8] Industrial analysis web site, e.g. <http://news.cnet.com/news/0-1006-201-4745832-0.html>
- [9] C. Lee, *et al.* Molecular Crystal and Liquid Crystal, 256(1994) 85
- [10] H. Ago, *et al.* Phys. Rev. B, 61(2000) 2286
- [11] M. Gao, *et al.* J. of Phys. Chem. B, 102(1998) 4096
- [12] M. Baraton, *et al.* Nanotechnology, 9(1998) 356
- [13] T. Nguyen, *et al.* Appl. Phys. Lett., 76(2000)2454
- [14] B. Schwartz, *et al.* Synthetic Metals, 116(2001) 35
- [15] Y. R. Shen, "The Principles of Non-linear Optics", New York: Wiley 1984
- [16] H. Mahr *et al.* Hirsch, Opt. Comm., 13 (1975) 96
- [17] J. Shah, IEEE J. of Quantum Electronics, 24 (1998) 276
- [18] Murray McCutcheon, M.Sc. thesis, University of British Columbia, 1999
- [19] US Patent # 5189136, N.N. Barashkov etc. Synthetic Metals 75 (1995) 153
- [20] A. P. Li, *et al.*, J. of Appl. Phys., 84 (1998) 6023
- [21] L. Rendu, *et al.* Opt. Materials, 17(2001) 175

- [22] Bing R. Hsieh, *et al.* *Macromolecules* 31(1998), 631
- [23] Junjun Wu, *et al.*, *J. Phys. Chem. B* 103(1999), 2374
- [24] D. Gin *et al.*, *Synthetic Metals* 101(1999) 52
- [25] E. Zojer *et al.*, *Synthetic Metals* 102(1999)1270
- [26] N.C. Greenham, R.H. Friend, *Solid State Physics*, 29(1995) 32
- [27] User's Manual, WinSpec, Princeton Instruments Spectroscopic Software, Version 2.4.M, September 20, 1999 Chapter11
- [28] <http://www.whatman.com>
- [29] K. Pichler *et al.* *J. of Phys.: Condensed Matter*, 5(1993) 7155
- [30] G. R. Hayes *et al.* *Synthetic Metals* 84(1997) 889
- [31] T. Nguyen *et al.* *Science*, 288(2000) 652
- [32] C. Y. Yanga, *et al.* *Synthetic Metals* 83(1996) 85
- [33] V. G. Dmitriev *et al.* "Handbook of Nonlinear Optical Crystals", Berlin: Springer, 1997
- [34] Personal communication with Dr. Katja Rademacher and Keri Kwong in M.O.Wolf's group
- [35] A. W. Ott *et al.*, *Chem. Materials*, 9(1997), 707
- [36] B. R. Hsieh, *et al.*, *Advanced Materials*, 7(1995), 36
- [37] A. K. Sheridan, *et al.*, *Synthetic Metals*, 111-112(2000), 531
- [38] R. Kersting, *et al.*, *J. of Chem. Phys.*, 106(1997), 2850
- [39] R. Kersting, *et al.*, *Phys. Rev. Lett.*, 70(1993), 3820

Appendix A

Maple code for calculating phase matching angle for BBO crystal cut at 38° .



```
restart;
```

```
n02:=proc(x);          # ordinary index squared for BBO
  2.7359+0.01878/(x^2-0.01822)-0.01354*x^2;
end;
```

```
ne2:=proc(x);          # extraordinary index squared for BBO
  2.3753+0.01224/(x^2-0.01667)-0.01516*x^2;
end;
```

```
lambdaG:=0.798;
```

```
lambdaPL:=0.610;
```

```
anglediff:=20.5;
```

```
phasematch:=proc(thetar)
```

```

local    kPL, kG, kS, nS,
         thetaM, lambdaS, theta2i, thetali, alpha, beta,
         thetalt, theta2t, gamma, thetam;

lambdaS:=(1/lambdaG + 1/lambdaPL)^(-1); # sum frequency beam
thetali:=thetar*Pi/180;
theta2i:=thetali - anglediff*Pi/180;
theta2t:=arcsin(-sin(theta2i)/sqrt(n02(lambdaG)));
thetalt:= arcsin(-sin(thetali)/sqrt(n02(lambdaPL)));
alpha:=theta2t - thetalt;
kPL:=sqrt(n02(lambdaPL))/lambdaPL: # PL beam wavevector
kG:=sqrt(n02(lambdaG))/lambdaG: # Gate beam wavevector
kS:=sqrt(kPL^2 + kG^2 - 2*kPL*kG*cos(Pi-alpha)); # Sum beam
nS:=kS*lambdaS; # Index of sum ray
beta:=arccos((-kPL^2 + kG^2 + kS^2)/(2*kG*kS));
thetam:= -38*Pi/180 + beta - theta2t;

(sin(thetam))^2 -
(1/nS^2-1/n02(lambdaS))/(1/ne2(lambdaS)-1/n02(lambdaS));

end:
angle:=fsolve(phasematch(thetar)=0,thetar); #Solve numerically for thetar
rotatefromgate:=anglediff-angle;
lambdaS:=(1/lambdaG + 1/lambdaPL)^(-1)*1000;

angle := 8.833027055

rotatefromgate := 11.66697295

lambdaS := 345.7244319

```

Appendix B

Maple code for calculating angular difference between the sum frequency propagation and the gate propagation, as a function of the PL wavelength. Wavelength of the gate is 798 nm. Angle between the gate and the PL is 18°.

```

restart;
n02:=proc(x);
    # ordinary index squared for BBO
    2.7359+0.01878/(x^2-0.01822)-0.01354*x^2;
end:

ne2:=proc(x);
    # extraordinary index squared for BBO
    2.3753+0.01224/(x^2-0.01667)-0.01516*x^2;
end:

lambdaG:=0.798;
anglediff:=20;
phasematch:=proc(thetar)
    local kPL, kG, kS, nS,
          thetaM, lambdaS, theta2i, thetai,
          alpha, beta, thetalt, theta2t, gamma, thetam;
    lambdaS:=(1/lambdaG + 1/lambdaPL)^(-1); # sum frequency beam
    thetai:=thetar*Pi/180;
    theta2i:=thetai - anglediff*Pi/180;
    theta2t:=arcsin(-sin(theta2i)/sqrt(n02(lambdaG)));
    thetalt:=arcsin(-sin(thetai)/sqrt(n02(lambdaPL)));
    alpha:=theta2t - thetalt;
    kPL:=sqrt(n02(lambdaPL))/lambdaPL; # PL beam wavevector
    kG:=sqrt(n02(lambdaG))/lambdaG; # Gate beam wavevector
    kS:=sqrt(kPL^2 + kG^2 - 2*kPL*kG*cos(Pi-alpha));
    # Sum beam
    nS:=kS*lambdaS; # Index of sum ray
    beta:=arccos((-kPL^2 + kG^2 + kS^2)/(2*kG*kS));
    thetam:=-cutangle*Pi/180 + beta - theta2t;
    (sin(thetaM))^2 -
    (1/nS^2-1/n02(lambdaS))/(1/ne2(lambdaS)-1/n02(lambdaS));
end:

Angle:=[seq(x[i],i=1..31)];
for i from 1 by 1 to 31 do
    lambdaPL:=0.550+(i-1)/200;
    PhaseMatching1:=fsolve(phasematch(thetar)=0,thetar);
    lambdaS:=(1/lambdaG + 1/lambdaPL)^(-1);
    thetai1:=PhaseMatching1*Pi/180;
    theta2i1:=thetai1 - anglediff*Pi/180;

```

```

theta2t1:=arcsin(-sin(theta2i1)/sqrt(n02(lambdaG)));
thetalt1:=arcsin(-sin(theta1i1)/sqrt(n02(lambdaPL)));
alpha:=theta2t1 - thetalt1;
kPL1:=sqrt(n02(lambdaPL))/lambdaPL;
kG1:=sqrt(n02(lambdaG))/lambdaG;
kS1:=sqrt(kPL1^2 + kG1^2 - 2*kPL1*kG1*cos(Pi-alpha));
nS1:=simplify(kS1*lambdaS);
beta1:=simplify(arccos((-kPL1^2 + kG1^2 + kS1^2)/(2*kG1*kS1)));
thetaS1:=simplify(beta1-theta2t1);
thetaOut1:=simplify(arcsin(-sin(thetaS1)*nS1));
Angle[i]:=simplify(anglediff-PhaseMatching1-thetaOut1*180/Pi);
od:
print(Angle);

```

```

10.68959556, 10.64635300, 10.60345869, 10.56090737, 10.51869484, 10.47681629,
10.43526706, 10.39404323, 10.35314017, 10.31255381, 10.27228097, 10.23231600,
10.19265726, 10.15329943, 10.11423950, 10.07547399, 10.03699892, 9.998810817,
9.960906510, 9.923282806, 9.885936326, 9.848863880, 9.812062344, 9.775527888,
9.739259016, 9.703251993, 9.667502964, 9.632010977, 9.596771544, 9.561783216,
9.527041740

```

Appendix C

Procedures for Silanization of Anodisc 13 purchased from Whatman Inc.

1. Place Anodisc under vacuum and heat to 100° C for 24 hours to remove residual moisture.
2. Under N₂ environment, add 0.1 ml of dry triethylamine to catalyze the reaction between alumina surface groups and silane. Then 1 ml trimethylchlorosilane was added to the Anodisc. The Anodisc was allowed to dark under N₂ for 2 hours and the excess was removed by vacuum.
3. Wash the Anodisc two times with dry hexane.
4. Dry the Anodisc and heat to 100°C for 1 hour under N₂.
5. Wash the Anodisc with ethanol and distilled water and dry under vacuum.